ABSTRACT

Title of dissertation: Three-Body Recombination and Rydberg Atoms in Ultracold Plasmas

Robert S. Fletcher, Doctor of Philosophy, 2008

Dissertation directed by: Professor Steven Rolston
Department of Physics

Ultracold neutral plasmas, created by photoionizing samples of laser-cooled atoms, have well-controlled initial density and temperature parameters. With initial particle peak densities of $\sim 10^{15}$ m^{-3}, initial ion temperatures in the tens of μK range, and initial electron temperatures with a controllable range of 1-1000 K, these systems provide a means to study otherwise laboratory-inaccessible parameter ranges for plasma research. Furthermore, these plasmas are inhomogeneous, unconfined, and freely expanding into a vacuum. Despite the extraordinarily low electron temperatures, the electron system remains weakly coupled, although the ion system exhibits strong coupling behavior.

While the initial electron temperatures are very low in ultracold plasmas, the temperature evolution has only been measured indirectly, in the earliest $\sim 5\%$ of the

plasma lifetime, and often with large uncertainties. We present a technique that, with further theoretical support, can provide straightforward temperature measurements throughout the first fifth of the plasma lifetime. By making use of collective modes of the plasma, we fit a model of Tonks-Dattner resonances (electron sound wave propagating in the plasma) to measurements of these resonances and obtain a time-dependent electron temperature measurement for the ultracold plasma.

Three-body recombination, a plasma loss process that has a rate scaling with the -9/2 power of the electron temperature, is of obvious interest in these ultracold plasma systems. Several theoretical works have predicted that the three-body recombination rate expression would need to be modified at these low electron temperatures, although the validity of these changes often hinges on the electron system being strongly coupled. We have performed the lowest temperature measurements of three-body recombination rates in a plasma and show that these measurements potentially provide a low-uncertainty means to calculate electron temperatures.

Three-Body Recombination and Rydberg Atoms in Ultracold Plasmas

by

Robert S. Fletcher

Dissertation submitted to the Faculty of the Graduate School of the
University of Maryland, College Park in partial fulfillment
of the requirements for the degree of
Doctor of Philosophy
2008

Advisory Committee:
Professor Steven Rolston, Chair/Advisor
Professor William Dorland
Professor Adil Hassam
Professor Howard Milchberg
Professor Luis Orozco

Table of Contents

List of Tables

List of Figures

Chapter 1

Introduction

First created at NIST-Gaithersburg, ultracold plasmas (UCPs) have become an important system for the study of low-temperature collisional processes. As a tool for exploring plasmas with otherwise difficult to obtain parameter ranges, UCPs are clearly invaluable as a means to expand knowledge of plasma physics to temperatures orders of magnitude colder than typically studied in plasmas. In particular, collisional processes and Rydberg-plasma interactions are easily studied in UCPs, as the relevant timescales of interest are increased (due to the low temperatures and low particle densities) to ranges easily handled in a laboratory. A process of particular interest is three-body recombination ($e^- + e^- + A^+ \rightarrow e^- + A^*$), whereby an electron facilitates the recombination of another electron and an ion into a weakly bound Rydberg atom. Typical three-body recombination (3BR) rates have the form:

$$R_{3BR}\,(s^{-1}) = K_{3BR}\,T_e^{-9/2} \int n_e^2(r) n_i(r) 4\pi r^2 dr, \tag{1.1}$$

and this rate expression will be addressed in detail in Chapters 3 and 4. The strong inverse dependence on electron temperature in this expression (a power of -9/2) highlights the interest in this process at low temperatures. The above rate expression was derived using Monte Carlo simulations for a fairly narrow range of particle energies [1]. Several theorists now consider the above equation to be possibly not applicable at low temperatures, depending on the degree of Coulomb coupling in

the electron system. Our work, in attempting to determine the validity of the 3BR rate expression above, makes the lowest temperature measurement of 3BR rates to date. Given errors in electron temperature measurements, however, the validity of the rate expression cannot be fully determined; instead, we show consistency between our measurements and other measured properties of the plasma. We make our 3BR measurements by direct observation of Rydberg atom populations in the UCP system. While field ionization ramps are a common technique for detecting Rydbergs, in our system the Rydberg atoms are embedded in a plasma and we must instead use microwave ionization pulses. This microwave technique, non-destructive to the plasma itself, has proven invaluable for these 3BR rate measurements.

The remainder of this chapter will address the creation of ultracold xenon plasmas as well as the basic techniques used to study them. Chapter 2 will discuss the temperature evolution of UCPs and the manner in which such temperatures may be measured. Rydberg processes in UCPs will be addressed in Chapter 3, and the specific process by which Rybergs are formed in UCPs (three-body recombination) and measurements of the rate of that process is addressed in Chapter 4.

1.1 Creation of the Xenon Ultracold Plasmas

The first UCP was created using a metastable xenon apparatus at NIST-Gaithersburg [2]; this apparatus has since moved to UMD-College Park and was used for the experiments described in this work. To create a UCP, we first produce a beam of metastable xenon atoms by running a DC discharge through a nozzle with

expanding xenon gas. After a differential pumping stage to reduce the pressure, an atomic beam with a metastable fraction of $\sim 10^{-4}$ is Zeeman slowed to reduce the velocity of the atoms in the beam to under 10 m/s. The atoms are then trapped in a magneto-optic trap (MOT). Using a two-photon photoionization process, the MOT atoms are then singly ionized, creating a neutral plasma.

The initial construction of this apparatus, for the purposes of creating a xenon time standard using a xenon MOT, was described in the Ph.D. dissertation of Matthew S. Walhout [3]. The apparatus has undergone several changes since its initial construction in 1994, but the basic concepts remain the same.

1.1.1 Source of Slow Metastable Xenon Atoms

A DC discharge of approximately 800 V at about 2 mA excites ground state xenon atoms at about 1×10^{-6} Torr to the $6s[3/2]_2$ metastable state; the expected efficiency from other, similar systems indicates this process likely results in .001% to .01% of the xenon being excited to the metastable level [3]. This state, with a lifetime of ~ 43 s (compared to our experimental cycle of 1 s), is needed for laser cooling and trapping techniques; the metastable state is effectively like a ground state alkali atom and has a cooling transition at 882 nm ($6s[3/2]_2$ to $6p[5/2]_3$ transition). Ground state xenon atoms have no such transitions that are accessible with current laser technology.

Differential pumping stages between the discharge and the Zeeman slower then reduce the pressure to about 2×10^{-7} Torr while also serving to collimate the

atomic beam. The Zeeman slower, consisting of a spatially varying magnetic field and a circularly polarized laser beam aligned with the field and anti-parallel to the direction of the atomic beam, reduces the velocities of the room-temperature atoms (about 240 m/s) to velocities a MOT can trap (10-15 m/s). The Zeeman slower beam is detuned about 135 MHz below the 0-Gauss 882 nm transition and the magnetic field spatially varies such that $kv_{\|} + \delta = \mu_B B_{\|}/\hbar$ is satisfied as the atoms traverse the length of the slower, where δ is the laser detuning from the zero-field transition, μ_B is the Bohr magneton, $k = 2\pi/882$ nm, $v_{\|}$ is the component of the atom velocity along the axis of the slower, and $B_{\|}$ is the magnetic field strength along the axis of the slower. The atoms absorb photons from the beam, are thus excited, then de-excite and emit photons in random directions, such that their forward velocities are reduced. However, as their velocities are reduced, the magnetic field likewise weakens (due to its position-dependence) such that the atoms are kept in resonance the entire time they traverse the Zeeman slower (per the equation above, Zeeman shift plus Doppler shift is always equal to the detuning of the laser beam). The atoms decelerate continuously until they reach the end of the slower, where the velocities are approximately 10-15 m/s. At this point the slowed atomic beam enters the experimental chamber of the vacuum system and is aligned such that the beam passes through the center of the MOT region.

The particular Zeeman slower in this apparatus is a reversed-coil configuration; that is, the field at the beginning of the slower is approximately 160 Gauss. About a meter along the slower, the field crosses zero and reverses direction, until it reaches -65 Gauss at the end of the slower (1.5 meters from the start of the slower, where

the sign is relative to the line pointing along the axis of the slower in the direction the atomic beam propagates)[3]. This is done by using two coils - the slower coil, providing the larger, positive field and running at about 35 A, and the reverse slower coil, providing the smaller, negative field and running at about 4.2 A. We use this configuration so that a smaller absolute field can be used (instead of a 225 to 0 G gradient, the zero point is shifted). Furthermore, this allows us to detune the slower laser beam so that it is not resonant with the zero-field transition the MOT uses; if the slower field tended toward 0 G at the end of the deceleration process, it is clear the slower laser would need to have a nearly 0 MHz detuning to compensate for the low-velocity Doppler shift at the end of the slowing process. In this case, the slower beam would resonantly push low velocity atoms, preventing MOT loading on the axis of the Zeeman slower. Our reverse-coil arrangement allows us to align the Zeeman slower axis with the MOT, as the slower beam only weakly interferes with the MOT due to the large 135 MHz detuning; this results in a more favorable MOT loading geometry. A diagram of the Zeeman slower is given in Fig. 1.1.

The magneto-optic trap consists of six laser beams arranged on three orthogonal axes in counter-propagating pairs, as well as a quadrupole magnetic field with a zero-field point at the intersection of the laser beams. The quadrupole field has a gradient of about 5 G/cm. Each beam is derived from a single Ti:Saph laser at 882 nm (detuned about 5 MHz from the zero-field $6s[3/2]_2$ to $6p[5/2]_3$ cooling transition and locked to this transition using saturated absorption spectroscopy in a xenon gas cell where metastable xenon is produced with an RF coil) and is about 2 cm in diameter and with about 8-10 mW per beam; each beam is circularly polarized such

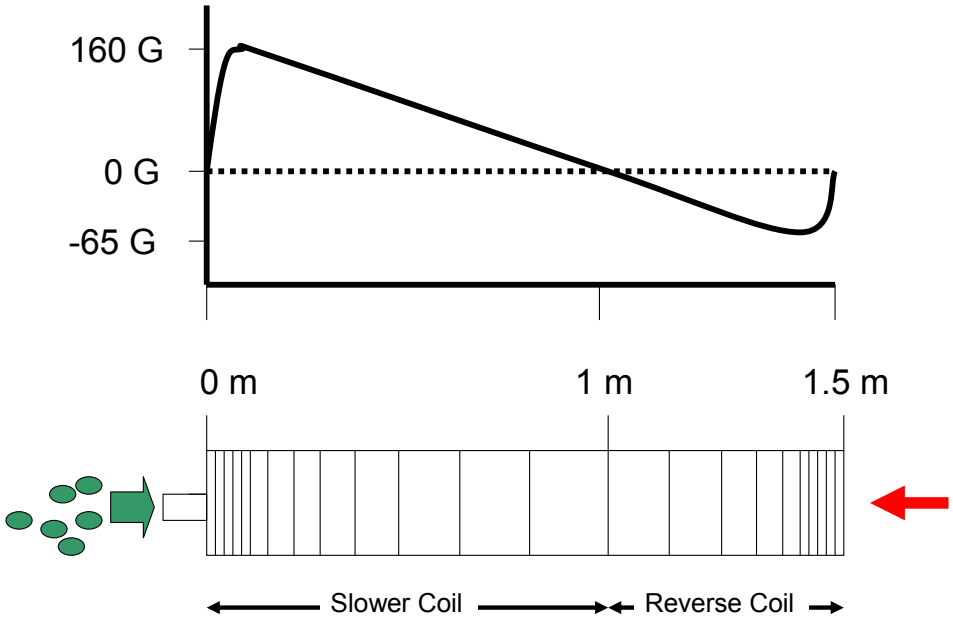

Figure 1.1: A schematic of the Zeeman slower. The atomic beam, on left, enters through a differential pumping cylinder. The Zeeman slower is a 1.5 m long cylinder with a varying-pitch magnet coil wound along its length. At the 1 m point, the reverse slower coil begins. The Zeeman slower laser beam enters from the right and is shifted 135 MHz from the zero-field resonance. A rough diagram of the axial magnetic field in the slower is plotted at top.

that atoms moving into a beam are Zeeman shifted into resonance with that beam. Note that the original MOT configuration in this system used three retro-reflected beams to create the total six beams; the current configuration uses four independent beams plus one retro-reflected beam. The reason for this beam configuration is due to geometries in the vacuum chamber; because we have wire-mesh voltage grids close above and below the plasma, four beams must pass through grids, such that retro-beams on those axes will be unbalanced (the forward beam is attenuated by the grids one time, while the retro beam passes through the grids three times before reaching the MOT region). However, we can retro-reflect along the third axis, as it passes between the grids and is not attenuated by them. We couple each of these beams into a polarization-maintaining fiber; on the output side of each fiber, we expand and circularly polarize the beams before they reach the MOT region. This trap is typically tuned for the Xe-132 isotope, which has no nuclear spin and thus the benefit of not requiring a repumper beam in the MOT. Furthermore, it is the most common of the bosonic species of xenon, resulting in faster MOT load times than other isotopes. The layout of the MOT is indicated in Fig. 1.2.

The physical principles with which a magneto-optic trap operates have been described in great detail in other references [4, 5]. Briefly, atoms in the intersection region of the six beams are trapped, as outward velocities will bring them into non-zero B-fields until the Zeeman shifts put the atoms in resonance with the beam they are moving into, providing a restoring force toward the center of the trap. A schematic of this in one dimension is shown in Fig. 1.3, and this can be generalized to three dimensions. While the resulting trap has a quadratic potential, viscous

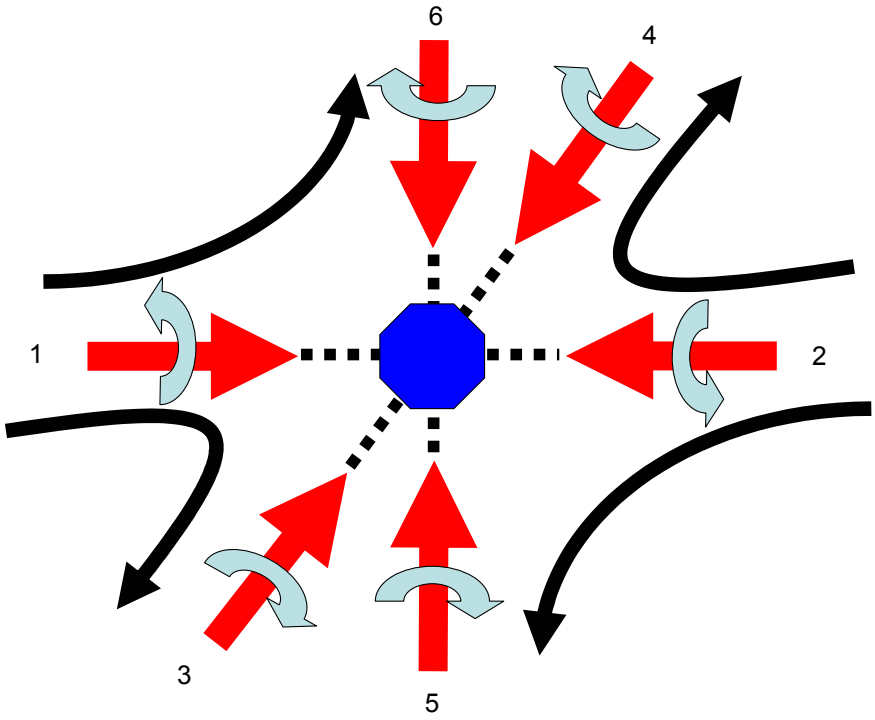

Figure 1.2: The MOT consists of 6 laser beams arranged along three orthogonal axes. The associated beam pairs are beams 1&2, 3&4, and 5&6. The MOT coils (not pictured) are co-axial with the 1-2 beam pair and are arranged in counter-current configurations, creating the quadrupole field (the curved arrows between beams). Note beams 3,4,5,6 are coplanar with one another and perpendicular to the 1-2 axis. The 1-2 beam pair carries one type of circular polarization based on the direction of the magnetic field relative to the direction of the 1-2 beams (the field is directed inward along with the beams); the other four beams, as the field is outward-going for them, carry the opposite circular polarization.

damping is provided by Doppler cooling effects, and the cooling has a lower bound determined by polarization gradient cooling effects [6]. Doppler cooling occurs when (in a 1-D system) an atom with a finite velocity preferentially absorbs photons from one or the other of two counterpropogating laser beams, when the preferential absorption is determined by the Doppler shift of the atom. Polarization gradient cooling is essentially an enhancement of that scattering rate (due to optical pumping of atoms into the M-sublevels that enhance scattering rates of photons from the beam the atom is moving into) and gives a lower bound on the MOT temperature of ~ 10 μK.

We allow the trap to load for approximately 800 ms; it reaches a steady state after about 500-600 ms, as the number of atoms in the trap is limited by Penning ionization (a density-dependent process where two metastable atoms collide, ionizing one and de-exciting the other as $Xe^* + Xe^{\rightarrow} Xe^+ + e^- + Xe$, thus losing both atoms from the MOT as the ground state is not trapped by the 882 nm MOT). It should be noted that this Penning ionization process can be utilized as a MOT diagnostic in this system, as the charged particles can be detected and used as a rough guide for optimizing size and density. The resulting atom cloud has a three-dimensional Gaussian density distribution. Typical parameters for the trap, as measured by time-of-flight and absorption imaging, are given in Table 1.1.

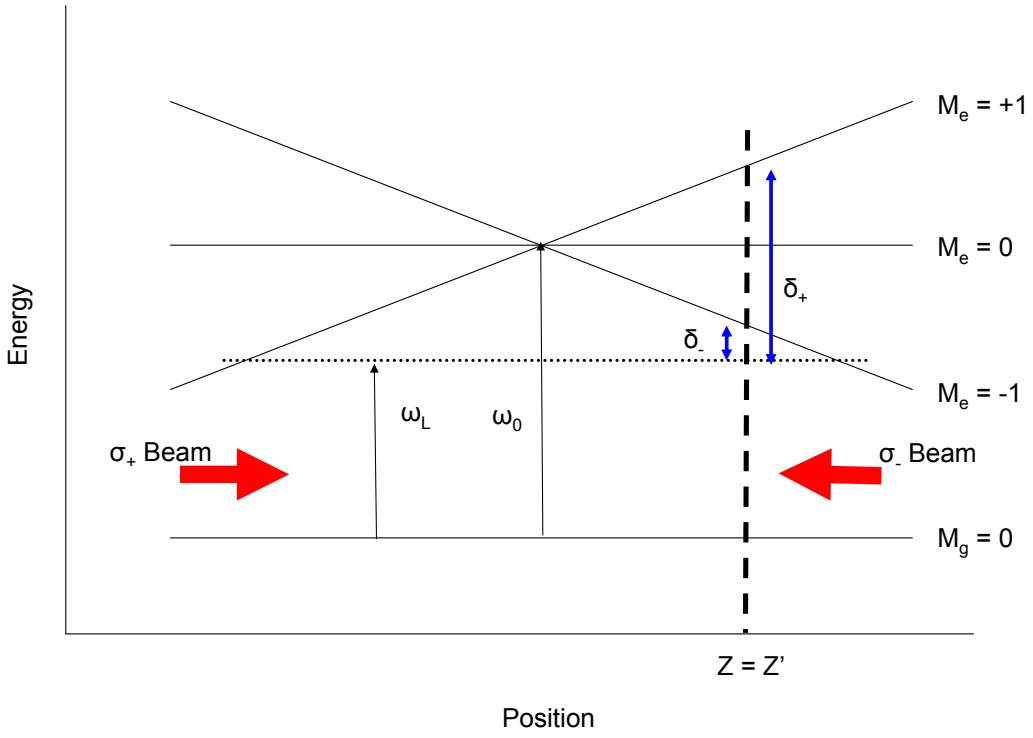

Figure 1.3: A schematic of a one-dimensional magneto-optic trap. ω_0 is the zero-Gauss 882 nm transition, while ω_L is the MOT laser frequency (detuned about 5 MHz from ω_0). An atom at position Z' has an excited energy level corresponding to the M_e=-1 curve due to the MOT magnetic field (not shown); such an atom is closer to resonance with the σ_- beam than the σ_+ beam, so it preferentially absorbs photons from the σ_- beam and is thus pushed back toward the center of the trap. Generalizing this to three dimensions results in three-dimensional confinement of the atoms.

Table 1.1: Magneto-Optic Trap (MOT) Parameters

Parameter	Abbreviation	Value
Temperature	T	$\sim$15 μK
Peak Density	n_0	2×10^{10} cm^{-3}
Radius	σ	280 μm

1.1.2 Creation of the Plasma

After the trap loading has reached a steady state condition, we photoionize the sample using a two-photon excitation process [2]. The first photon, at 882 nm, is supplied by the MOT beams (shifted onto resonance for the 0 G $6s[3/2]_2$ to $6p[5/2]_3$ transition). The second photon, at 514 nm, is supplied by a 10 ns pulse from a Nd:Yag pumped dye laser with a bandwidth of $\sim$ 0.1 cm^{-1}. Note that the entire experiment is clocked off of the 10 Hz pulse laser, so it is quite easy to synchronize the green and IR pulses. We run the experiment itself on a 1 Hz cycle, so that every tenth pulse is used for ionization; the other nine pulses per cycle are blocked with a copper-plated mechanical shutter placed between the Nd:Yag and the dye laser to increase the effective dye lifetime. The IR pulse is typically switched on very shortly before the green pulse and is set to be longer in duration than the green pulse, so that any jitter in the timing electronics will have negligible effect on the photoionization process; while these timings vary, we often set the red pulse to be about 100 ns in duration with the green pulse centered at the 50 ns point.

Upon ionization, the electrons receive nearly all of the surplus energy in

the green photon (the energy carried by the photons in excess of the ionization energy), due to the large mass difference between the xenon ions and the electrons ($E_e = \left(\frac{m^*_{Xe}}{m^*_{Xe}+m_e}\right)\Delta E$, where ΔE is the surplus energy in the green photon). The ion system starts at roughly the same temperature as the MOT atoms ($E_i = \left(\frac{m_e}{m^*_{Xe}+m_e}\right)\Delta E$), although a large ΔE can result in ion temperatures near 1 mK. By tuning the dye laser frequency, we can control the energy of the 514 nm photon so that the resulting electron system has an energy ranging from 0.1 K to 1000 K (although initial electron temperatures effectively end up to be at least 1 K due to fast heating effects immediately after ionization). We can also tune below the ionization threshold and create a dense gas of Rydberg atoms. Typical initial plasma parameters given in Table 1.2.

Table 1.2: Ultracold Plasma (UCP) Parameters

Parameter	Abbreviation	Value
Initial Ion Temperature	$T_i(0)$	$\sim$15-1000 μK
Initial Electron Temperature	$T_e(0)$	1-1000 K
Peak Density (r=0, t=0)	$n_i(0,0)$ and $n_e(0,0)$	2×10^9 cm^{-3}
Radius	σ	280 μm
Asymptotic Expansion Velocity	v	45-100 m/s

Note that the ion and electron density distributions are initially equal to one another. Both distributions are likewise identical to the original MOT distribution with a multiplicative scaling factor to account for the maximum 2-photon ionization

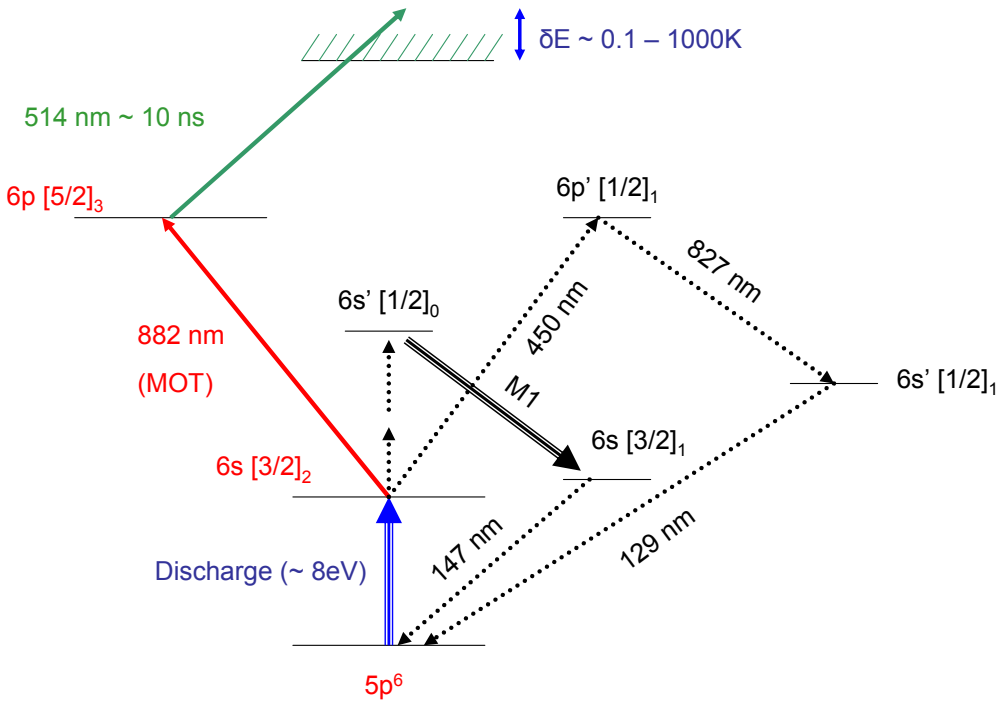

Figure 1.4: The xenon energy levels of interest to this work are on the left of the plot (the discharge, 882 nm, and 514 nm transitions). A DC discharge excites ground state xenon to the $6s[3/2]_2$ metastable level. The MOT operates on the cooling transition at 882 nm. A two-photon ionization process, using the 882 nm photons together with 514 nm photons from a pulsed laser singly ionizes the xenon, resulting in a neutral plasma with variable initial electron energies.

efficiency of $\sim 25\%$. The actual number of atoms photionized can be controlled by varying the pulse intensity of the 514 nm pulse.

1.2 Xenon Ultracold Plasma Characteristics

1.2.1 Plasma expansion

Upon creation of the plasma, the electron system is substantially warmer than the ion system. The electron cloud then begins to expand, exerting an outward force on the ions. A small number ($\sim$2-3%) of electrons escape the plasma, resulting in a slight macroscopic positive charge for the overall system. This charge imbalance serves to create a confining potential well for the remaining electrons. When this well depth becomes greater than the average electron kinetic energy, the remaining electrons are trapped, forming a neutral plasma. Self-consistent models of the charge distributions for typical plasma parameters and charge imbalances indicate the electron density distribution will closely follow that of the ions; thus for most applications we may use the approximation:

$$n_e(r,t) \sim n_i(r,t) \sim \frac{n_i(0,0)\sigma_0^3}{\sigma(t)^3} exp[-r^2/2\sigma(t)^2] \tag{1.2}$$

where r is the distance from the center of the plasma and $\sigma(t) = \sqrt{v^2t^2 + \sigma_0^2}$. This self-similar expansion has been experimentally verified [7, 8]. Some simulations indicate deviations in this approximation of the density distributions, but the deviations are typically fairly minor and limited to the large-radius, low-population region of the plasma.

A far more significant deviation is expected due to the continued evaporation of electrons from the system and the resulting charge imbalances. A good approximation of this effect on the distributions is to simply assume the ions continue to expand with a distribution described by Eq. 1.2, while the electron distribution is identical to the ion distribution, but with a truncation at the appropriate radius such that the total electron number is correct - that is, as electrons are lost to evaporation (due to a weakening of the confining potential due to expansion), by rough approximation they are simply lost from the outermost regions of the plasma, while the interior of the plasma tends to maintain an electron distribution very similar to the ion distribution. This is simply a feature of the very low electron temperatures; the potential seen by the electrons is deep compared to the electron temperatures, so that they tend to occupy the middle of the potential, and adjust their density distribution to match the ion density distribution.

A significant difference between Eq. 1.2 and the actual plasma expansion occurs at early times in the expansion. The plasma actually expands at an accelerating velocity due to electron pressure effects. Thus the single, constant velocity used in Eq. 1.2 (in the $\sigma(t)$ term) is actually only valid after about 10 μs, at which time the plasma expansion velocity is very close to an asymptotic expansion velocity. Before this time, the expansion velocity is somewhat lower than v, albeit increasing due to the electron-pressure-driven acceleration.

The most interesting predicted deviation from Eq. 1.2 is the formation of an ion shock wave in the plasma [9]. In fluid model simulations, this is observed to form at a fairly large radius in the plasma ($\sim$ 3-3.5 $\sigma(t)$). Unfortunately, it appears

that such a feature will be very difficult to detect in ultracold plasma systems, due to the small number of charge carriers involved and the narrowness of the resulting ion density spike. This ion shock wave may account for other features in the plasma; this is briefly discussed in Section 2.3.4.

Plasmas with a very large initial charge imbalance will undergo a Coulomb explosion effect instead of an electron-pressure driven acceleration [10]. These plasmas, which are formed by ionizing a much smaller number of atoms than the other UCPs addressed in this work, do not have a sufficient number of ions to retain electrons. All of the electrons leave the plasma upon ionization, leaving a single-species ion plasma, which then expands at an accelerating velocity due to Coulomb forces.

1.2.2 Evaporation and Neutrality

As briefly mentioned in Section 1.2.1, electrons evaporate from the plasma. Because of the charge imbalance in the plasma, the electrons are in an attractive potential; however, the warmer electrons are able to leave the system and thus cool the plasma. We can perform self-consistent calculations for the plasma potential as a function of the charge imbalance and electron temperatures. The basic technique is as follows. First, we assume initial distributions by calculating the ion and electron distributions for the particular expansion time t using Eq. 1.2. Based on the measured charge imbalance (discussed later in this section) at that time t, we truncate the electron distribution at the appropriate radius such that the resulting electron distribution, integrated over all space, gives the appropriate number of elec-

trons for the particular charge imbalance. We then begin to iterate the code over the following equations:

$$\frac{1}{r}\frac{\partial^2}{\partial r^2}[rU(r)] = -\frac{e^2}{\epsilon_0}[n_i(r) - n_e(r)] \tag{1.3}$$

$$n_e(r) = \alpha \exp\left[\frac{U(r)}{k_B T_e}\right] \tag{1.4}$$

$$\alpha = N_e / \int 4\pi r^2 \exp\left[\frac{U(r)}{k_B T_e}\right] dr \tag{1.5}$$

where Eq. 1.3 is Poisson's equation, solving for the potential $U(r)$ for a given charge distribution $n_i(r) - n_e(r)$. Equation 1.4 assumes a Boltzmann distribution for the electron system, although in practice we truncate this distribution at high energies at each iteration of the code with either a quadratically varying cut (as in [9]) or a Michie-King type cut (see Fig. 4.1). Equation 1.5 renormalizes to keep the total number of electrons N_e constant. On each iteration, the n_i is kept constant and the new n_e is obtained by adding a few percent of the newly calculated n_e to the n_e of the previous step; adding more than a few percent will result in a diverging solution. Iterations are repeated until the calculated n_e converge to a satisfactory degree. In this manner, estimates for the potential $U(r)$ that the electrons in the plasma are subjected to can be calculated (an example result is plotted in Fig. 3.5a).

We can easily measure the total charge imbalance in the system. After detecting the electron emission from the plasma (described in Section 1.3, with a typical emission curve shown in Fig. 1.8), where $P(t)$ is the time dependent emission curve, the fraction of electrons remaining in the plasma as a function of time ($M(t)$) is simply

$$M(t) = 1 - \frac{\int_{t'=0}^{t'=t} P(t')dt'}{\int_{t'=0}^{t'=t_{max}} P(t')dt'} \tag{1.6}$$

where $t = 0$ is the start of the plasma and t_{max} is the time at which the plasma electron emission curve has ended (typically around 200 μs). Note that ions also evaporate from the system, and a similar measurement may be done of the ion loss as a function of time; however, the time scale over which ions leave the plasma is much longer than that for electron evaporation, so typically only the electron loss measurement is needed for estimating the neutrality. An example of the resulting measured fractional particle population vs. time is given in Fig. 1.5. The neutrality is approximately just the fraction of electrons remaining in the system, as ion loss is comparatively slow. This time-dependent neutrality is used for any measurements requiring an estimate of the number of electrons in the system at a particular time; namely, the Rydberg population measurements of Section 3.3.2 and Chapter 4.

1.2.3 Plasma Parameters of Interest

Note that the inhomogeneous (Gaussian) density distribution of our UCP has several ramifications on calculations. For example, the cold plasma resonance frequency is proportional to $n_e^{-1/2}(r)$ and will have spatial variation across the plasma. Similarly, the Debye length

$$\lambda_D(r) = \sqrt{\frac{\epsilon_0 k_B T_e}{n_e(r) e^2}} \tag{1.7}$$

varies within the plasma. Thus the central core of the plasma, as well as being the most charge-neutral region of the plasma, is also most clearly within the plasma realm (based on Debye lengths); on the fringes of the plasma, the Debye length becomes comparable or greater than the 1-σ size of the plasma, see Fig. 1.6. Recalling

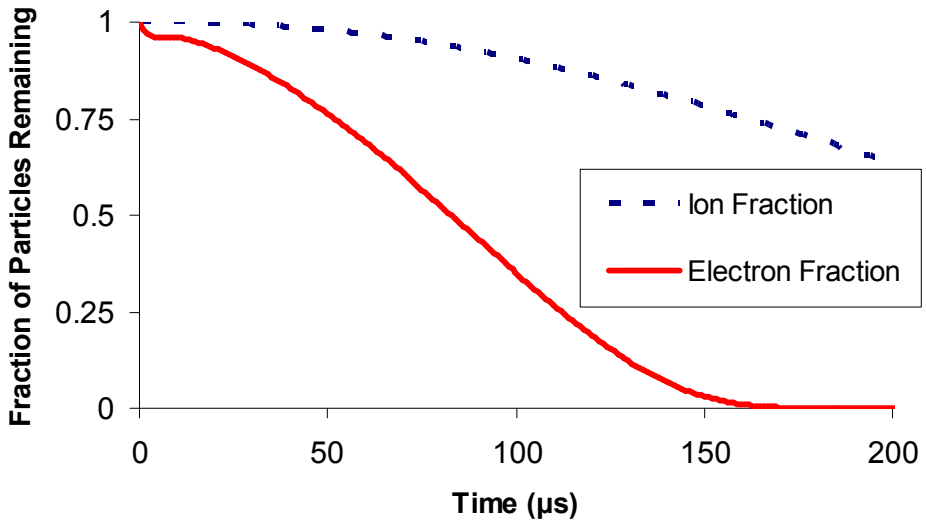

Figure 1.5: Fractions remaining of the ion and electron systems. Because of the long timescale of ion loss, the ion population can typically be considered to be constant, so that the fraction of electrons remaining is effectively the neutrality of the system.

that standard definitions of a plasma require the Debye lenth to the larger than the size of the plasma, it is clear that this system satisfies this plasma definition (except possibly on the very fringes of the plasma, where only a small fraction of the particles are located).

A standard plasma parameter of interest is the Coulomb coupling parameter:

$$\Gamma = \frac{e^2}{4\pi\epsilon_0 a k_B T} \propto \frac{n^{1/3}}{T} \tag{1.8}$$

where e is the electron charge, $a = (3/4\pi n)^{1/3}$ is the Wigner-Seitz radius with n and T as the density and temperature of the particles (this quantity can be calculated for either the electrons or the ions in the system by using the appropriate n and T). A $\Gamma > 1$ indicates a strongly coupled system, which is a "'non-ideal"' plasma where correlations become important, while $\Gamma < 1$ indicates a weakly coupled, ideal plasma. Initial focus on UCP systems hinged on the possibility of creating a strongly-coupled system. However, subsequent work (both theoretical and experimental) indicates the electrons are nearly always in the weakly-coupled regime (they may be strongly coupled immediately on ionization, but early strong heating effects push them into the weakly-coupled regime almost instantaneously [11] or 3BR heating prevents strong coupling [12]) and the ions are only moderately strongly coupled, with a Γ of about 1-4. Substantial work has been done to address the possibility of strong coupling in UCPs [13, 14], as the Coulomb crystallization that can occur at very high values of Γ is of ongoing interest [15].

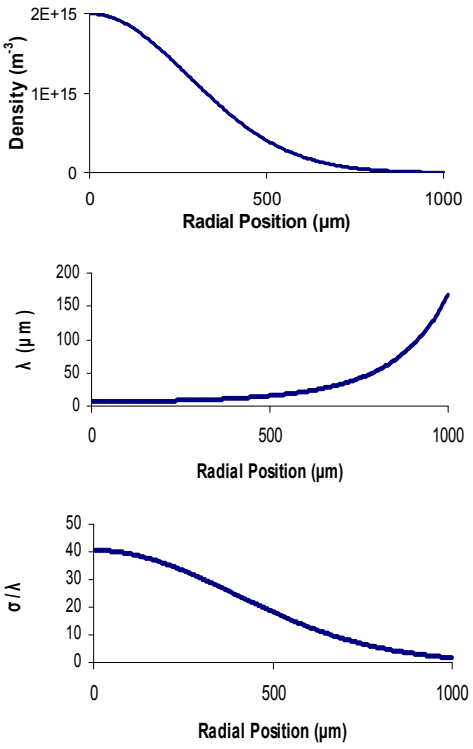

Figure 1.6: For T_e=20 K, $n_e(0,0) = n_i(0,0) = 2 \times 10^{15}$ m^{-3}, $t = 0$, and $\sigma = 280$ μm, the top plot is the electron density distribution as calculated by Eq. 1.2. The middle plot is the corresponding position-dependent Debye length $\lambda(r)$, calculated with Eq. 1.7. The bottom plot is the ratio of the 1σ size of the plasma (280 μm) to the Debye length as a function of radius.

As the plasma expands, the temperatures of both the ion and electron systems change due to various heating and cooling effects. This, together with the measured Coulomb coupling parameters of UCPs, is discussed in Chapter 2.

1.3 Available Probes of Ultracold Plasmas

The techniques available for studying ultracold plasmas are relatively limited. Xenon ions do not have easily accessible optical transitions, so various imaging techniques (absorption and flouresence) are not feasible. Due to the small size of the sample and the low number of charge carriers, solid electrode-based probes are not suitable.

The primary measurement tool available for our xenon plasma is a multi-channel plate (MCP) detector located approximately 15 cm below the plasma. Using a series of grids with varying voltages, we can accelerate either electrons or ions to the detector (Figure 1.7). The result is a time-dependent current proportional to the number of particles hitting the detector (Figure 1.8); electrons are typically studied in this manner, as they are constantly emitted from the plasma through an evaporative process (as the plasma expands, the potential that arises due to the ion-electron imbalance weakens, so that the warmer electrons are able to escape). However, by changing the grid bias voltages, the MCP can also be used to detect ions, which are emitted from the plasma on a much longer timescale than the electron emission. The MCP also has a phosphor screen, allowing us to obtain spatial

information regarding where on the detector charged particles strike. By estimating charge lensing effects due to the guide grids, this information can be used to extract the size of the plasma at various times. See Appendix A for a description of this technique.

The MOT itself can be measured using typical optical techniques. Absorption imaging and time-of-flight measurements can be used to determine the approximate size and temperature of the initial MOT.

1.4 Other Ultracold Plasma Experiments and Related Work

1.4.1 UCPs

The properties of UCPs are roughly independent of the elements used to create the plasmas. Our use of xenon is historical, as it was an available system when UCP research started. Recent UCP experiments have been performed with alkaline earth elements (namely calcium and strontium), as the ions have optical transitions that are easily laser accessible (the xenon ion transition is in the vacuum ultraviolet)[16, 17]. The Ca and Sr plasmas are somewhat larger and denser than the xenon plasma, but otherwise behave in a very similar (up to the scaling) manner. The major benefit of using these elements is that the optical transitions can be used to image the plasma ions using either absorption or flouresence imaging. An added benefit is the possibility of further cooling the ions in the plasma, by use of the cooling transition used for imaging; this has not yet been demonstrated.

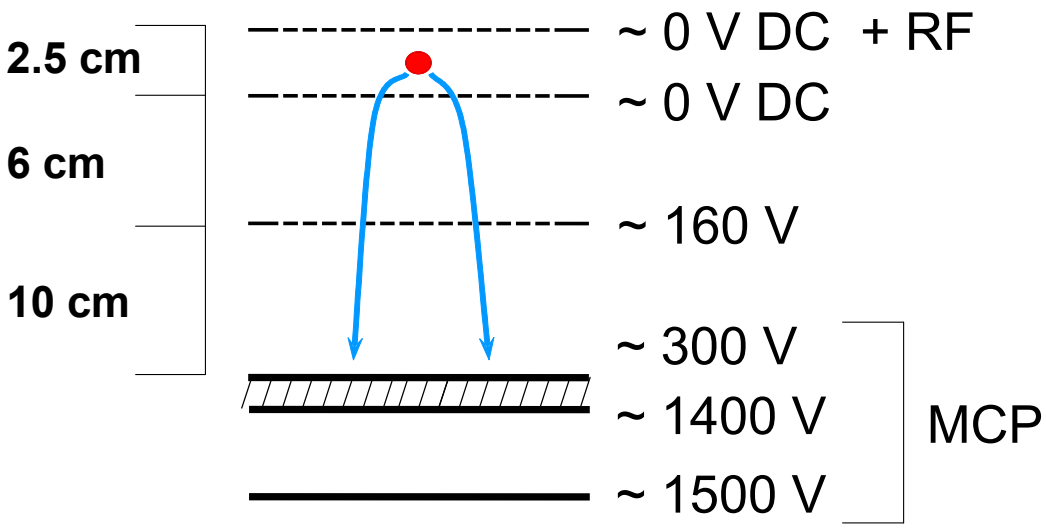

Figure 1.7: A diagram of the MCP and guide grid geometry. The plasma (red dot) emits electrons (blue, arcing lines) as it expands. The grids immediately above and below are biased at a few mV in such a manner as to attempt to shield the plasma from external fields while still maintaining a slight bias so that emitted particles are directed down toward the MCP. Either of those grids can have RF or microwaves coupled on top of the small DC bias. The middle grid (shown here at 160 V) typically is biased at a few hundred volts to assist in guiding particles to the MCP. The front of the MCP is typically biased at a few hundred volts (often ∼300 V) and the back of the MCP and the phosphor screen are typically biased at 1300-1500 V.

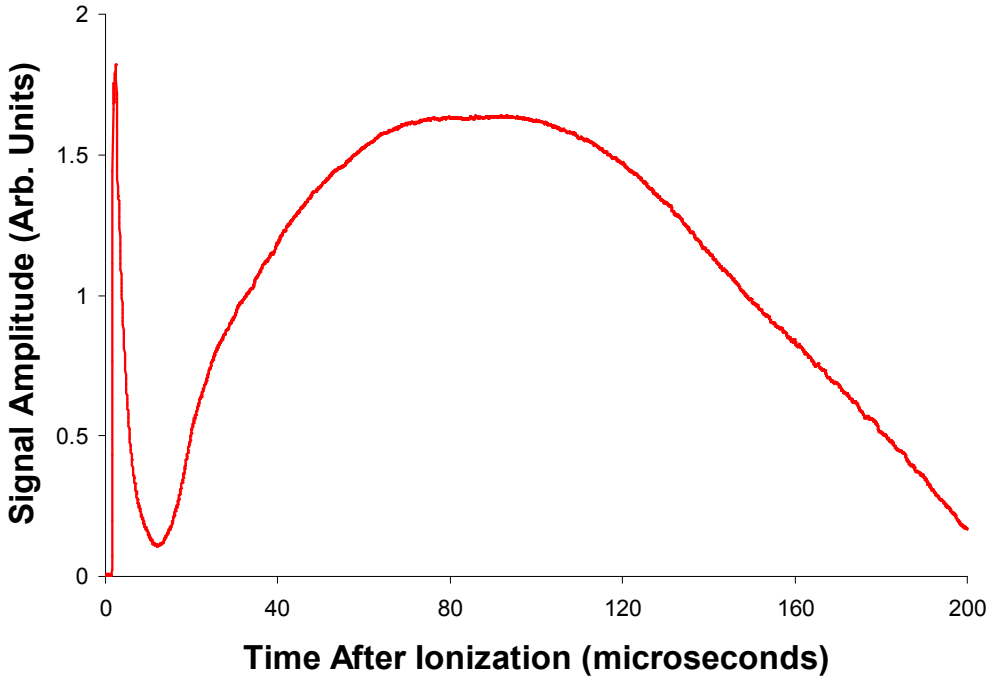

Figure 1.8: A sample electron emission curve using the MCP. The first tall, narrow peak (at t=0 μs) is the initial loss of 2-3% of the electrons immediately after ionization. The broad peak (t=20 to 200 μs) is the electron evaporation curve that results from the free expansion of the plasma.

1.4.2 Rydberg Gases

Dense Rydberg gases are closely related to ultracold plasmas, as the two types of systems can evolve easily from one to the other [18, 19, 20, 21, 22]. In a UCP system, the photoionization process can be tuned to just below the ionization threshold and can actually target particular Rydberg levels in the atom. The resulting cloud of highly excited atoms will then quickly evolve into a UCP, as Rydberg-Rydberg collisions ionize some Rydbergs and the resulting electrons proceed to ionize the rest of the sample in a cascade. Similarly, a UCP produces Rydbergs through three-body recombination, due to its modest densities and very low temperatures. While the UCP never converts fully to a Rydberg gas, it produces a substantial number of Rydbergs that persist beyond the time at which the UCP is fully dissipated.

1.4.3 Anti-hydrogen Production

Currently, the production of anti-hydrogen involves the use of two ion traps, one for positrons and one for anti-protons. By then superimposing the trapped populations, a neutral ultracold plasma is the effective result; neutral anti-hydrogen is then produced via three-body recombination [23, 24]. With parameters similar to those of the xenon UCP, this anti-particle trap exhibits similar characteristics and there is considerable interest in using UCP systems to study effects in these anti-particle plasmas. Direct comparisons between the two types of plasmas must be done carefully, however, as the anti-particle plasmas are in very strong magnetic fields (on the order of 1 Tesla).

Chapter 2

Temperature Measurements

2.1 Overview

A fundamental issue in ultracold plasma physics is the determination of the particle temperatures in the plasma. While several studies have been conducted to determine the ion temperatures of UCPs (based on measurements of the plasma expansion velocities), the measurement of the electron temperature is more difficult. To date, such measurements have relied on difficult experimental techniques with limited accuracy or heavy simulation work. Good knowledge of electron temperatures is fundamental to the understanding of UCPs; for example, the strong T_e dependence of the three-body recombination rate expression clearly indicates that low-temperature experimental verification of that rate expression is contingent on accurate measurements of T_e. Furthermore, knowledge of particle temperatures is required to determine the degree of Coulomb coupling each species is subjected to; this is of interest, as strongly- and weakly-coupled plasmas behave in substantially different ways and would thus require different types of theoretical treatments.

2.2 Ion Temperatures

Xenon ions are not directly observable, as the optical transitions from the ground state of Xe^+ are deep in the vacuum ultraviolet and thus very difficult to access with current laser technology. Other UCP systems, using strontium or calcium, have optical transitions at currently accessible wavelengths (for example, 422 nm for Sr^+ and 397 nm for Ca^+) and can therefore use either absorption imaging [16] or fluorescence imaging [17] to determine the size of the ion cloud as a function of time. Thus, the expansion velocity of the ion system can be determined directly, providing an indirect measurement of the ion temperatures. We are currently exploring a third technique: because the MCP in our xenon system has spatial readout in the form of a phosphor screen, it has the potential to be a more versatile tool for observing the time-dependent size of the ion (or electron) system than either absorption imaging or fluorescence imaging (see Appendix A for examples of this MCP imaging technique). This is due to the high sensitivity of the MCP to charged particles; using the MCP, we can image the ion distribution at far later times than either absorption or fluorescence imaging can effectively observe the ions. While ion temperature effects are only of peripheral concern for the projects addressed in this work, they are included here for completeness. In general, all ion temperature measurements indicate the ion system is moderately strongly coupled with a coupling parameter $\Gamma \sim 1 - 4$,

2.2.1 Disorder-Induced Heating

Very early in the plasma lifetime, disorder-induced heating in the ion system is observed [16]. This strong, but short-lived, heating process is explained when one notes that, immediately following the photoionization event, the system has gone from a collection of neutral particles to a collection of ions and electrons [25]. These charges are not formed in the spatial distribution that minimizes the potential energy, but are instead randomly distributed due to the initial random positions of atoms in the MOT. As the ions and electrons shift to minimize the local Coulomb interaction, the plasma heats. The ions quickly heat up from their initial ~ 15 μK temperature to about .5-2 K, depending on initial conditions such as the MOT density. The electron system also undergoes disorder-induced heating, although at a very fast rate (effectively instantaneously upon ionization; that is, during the ionizing laser pulse), leading to an effective lower bound on the t=0 electron temperature of a few Kelvin regardless of how small we set the surplus energy in the photons.

One aspect of disorder-induced heating in the ion system is that the process takes several microseconds. In this time, the ions actually tend to over-compensate and develop a small oscillation in kinetic energy [26]. This oscillation damps out fairly quickly, however. As this ion energy oscillation is fully damped within about 5 μs after ionization, it is a very limited effect. It is, however, an indication of the strongly-coupled nature of the ion system.

2.2.2 Temperature Equilibration

Perhaps the most important feature of ion temperature behavior as it pertains to three-body recombination work is also the least surprising behavior: thermal equilibration with the electron system. As in any collisional system with two species of particles at differing temperatures, the ion and electron systems in UCPs gradually come to thermal equilibrium. This is, however, a slow process due to the relatively low rate of electron-ion collisions as every transfer of energy is low due to the mass difference; equilibration takes on the order of several hundred μs. This results in the ion system slowly heating and the electron system slowly cooling. Using the relationship given in [27], the xenon ion-electron equilibration time for densities $n = 1 \times 10^9$ cm^{-3}, $T_e = 10$ K, and $T_i = 1$ K has a value of about $1/\ln(\Lambda)$ ms, where $\ln(\Lambda)$ is the Coulomb logarithm (Λ is the ratio of the Debye length to the Thomson radius, $e^2/k_B T_e$). The Coulomb logarithm, while noting it is often only correct to factors of order 1, is approximately 1.8 for the parameters listed, giving temperature equilibration times on the order of 570 μs. Note that this is an initial electron-ion equilibration time; as the plasma expands and the electron system cools, these equilibration times will increase. As the plasma fully dissipates within 200-250 μs, the electron and ion systems are not expected to fully equilibrate at any point in the plasma lifetime.

2.3 Electron Temperatures

The electron temperatures in an expanding UCP are expected to be influenced by a wide variety of effects. The electrons are subject to very early disorder-induced heating and slow (and incomplete) equilibration with the ions. Furthermore, there is some heating due to the creation of Rydberg atoms, and the subsequent Rydberg-electron collisions can further influence the electron temperature. As the plasma expands, the electron system undergoes adiabatic cooling, because the expansion is driven by the electron pressure on the ion system. Throughout the expansion of the plasma, hot electrons leave the system, resulting in an evaporative cooling effect.

Direct measurement of the electron temperature in UCPs is a difficult problem. This is largely due to the nature of the UCP system; given its small size (hundreds of μm) and low number of charge carriers ($\sim$500,000 electrons at creation), the use of standard plasma probes is not feasible. Instead, new techniques must be developed and employed to extract information regarding this particular plasma parameter.

2.3.1 Modeling Techniques

Given the experimental difficulty associated with an electron temperature measurement in UCP systems, several groups have developed plasma models to estimate the electron temperatures [9, 11, 28, 29, 30, 31]. These time-dependent models have a large number of input parameters and are very complex due to the number of processes affecting the ions, electrons, and the interactions between the two species. Because of this, simulation results can vary. While these results are useful, there is

an obvious desire to confirm the predicted electron temperature curves with direct measurements of the temperatures. This is of added importance when one considers the large number of open questions remaining in UCP studies, particularly pertaining to electron behavior, which makes heavy reliance on simulation results non-ideal.

2.3.2 Spilling Techniques

The first direct electron temperature measurement was performed at NIST-Gaithersburg in 2004. By applying a weak electric field to the plasma, the potential well that the electrons in the system respond to will be tipped, allowing the hot electrons in the plasma to leave the system [32]; that is, the electric field's linear potential, when summed with the plasma potential, creates a saddle point that allows electrons with sufficient energy to leave the plasma (Fig. 2.1). By measuring these exiting electrons as a function of the tipping field applied and assuming a Boltzmann distribution for the electrons, an estimate of the electron temperature can be made:

$$f = \beta + \lambda \int_{E_{cut}(F_0)}^{E_{cut}(F)} D(\epsilon)\exp(-\frac{\epsilon}{k_B T})d\epsilon \tag{2.1}$$

where f is the fraction of the plasma electrons spilled as a function of F, F is the applied field amplitude, E_{cut} is determined by F per Fig. 2.1, λ and β are fit parameters corresponding to the chemical potential and a background subtraction, and $D(\epsilon) = [\kappa^3(2m_e)^{3/2}]/16\hbar^3|\epsilon|^{5/2}$ is the density of states for the potential seen by

electrons in the plasma, calculated in its asymptotic limit [32], where the electron potential $U \sim -\frac{\kappa}{r}$.

This technique was successful at measuring the electron temperatures (Fig. 2.2(a)). However, it is only applicable early in the plasma lifetime; after about 10 μs, the emitted electron signals are no longer useful; this is because after this time, the plasma has expanded sufficiently so that the saddle point created by an external field is in the $1/r$ part of the plasma potential (that is, the far-field potential), violating an assumption that leads to Eq. 2.1. Furthermore, since the electrons in this finite-depth potential obviously cannot have a true Maxwell-Boltzmann distribution, this technique requires careful modeling of the plasma density distribution and appropriate treatment of the truncated Maxwell-Boltzmann distribution as well as the proper calculation of the density of states. As a result, the temperature measurements have fairly large uncertainties.

In Figure 2.2(b), the electron Coulomb coupling parameter associated with the measured temperatures is plotted. Recall that the Coulomb coupling parameter Γ is the ratio of the electron Coulomb energy to the electron kinetic energy and thus serves to measure the degree of coupling of electrons to other electrons in the system. A Γ in excess of 1 indicates a strongly coupled system; in such a system, plasma dynamics change substantially, as correlations become important. In particular, the collisional rates addressed elsewhere (namely three-body recombination) are derived under the assumption that $\Gamma << 1$. Because the electron Γ values measured in UCPs are consistently well below unity, modifications to those rate expressions due to strong coupling need not be considered.

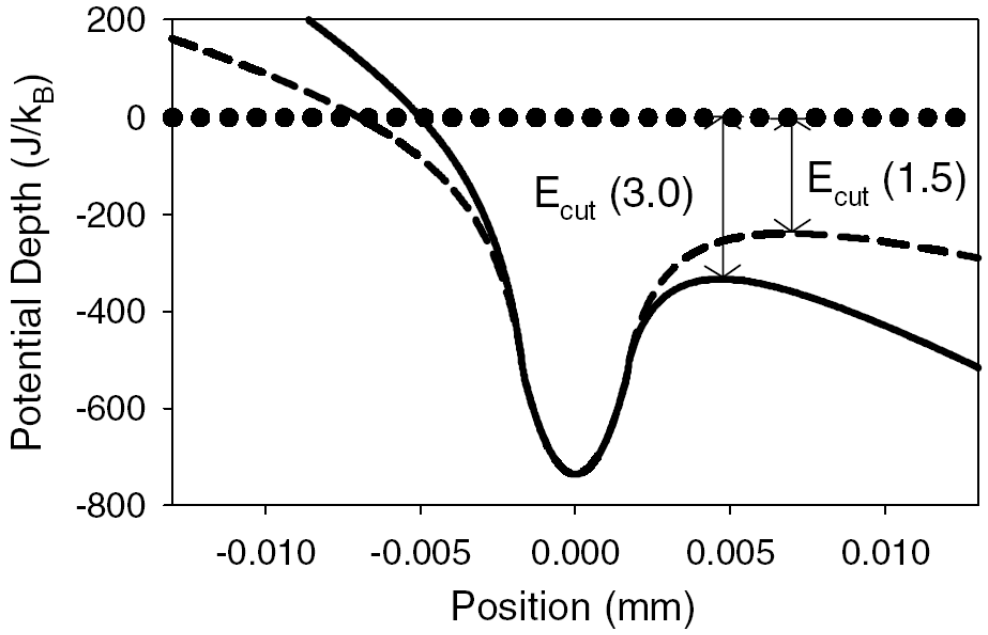

Figure 2.1: A schematic of the potential tipping scheme. Hot electrons in the plasma are spilled out of the system and measured, allowing the electron velocity distribution to be sampled and thus determining the electron temperature. The electron potentials plotted are the self-consistent solutions along the direction of the external applied electric field at applied fields of 1.5 and 3.0 V/m. The saddle points (locations of the arrows) determine the energy at which the electron Boltzmann distribution is cut by the external field. From [32], used with permission.

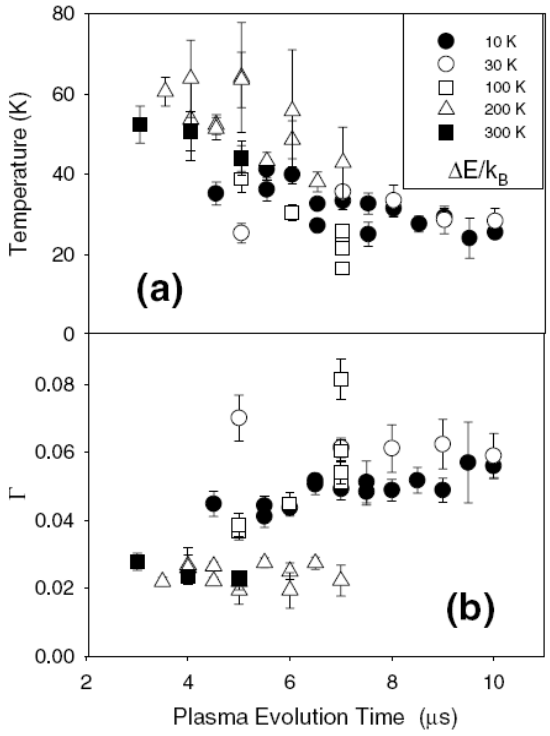

Figure 2.2: (a) The electron temperatures measured using the electron spill technique for varying initial electron energies. (b) The calculated Coulomb coupling parameters Γ associated with the temperature measurements indicated in (a). From [32], used with permission.

2.3.3 Using Ion Temperature Measurements

As previously noted, there have been multiple measurements of the ion temperatures. A complete simulation of the plasma, including energy sources and sinks for the electrons and ions, can use the ion temperature measurements as verification of the simulation. Electron temperatures can thus be estimated using such a verified simulation [33]. While this technique has promise, its validity is still only as good as the assumptions used in the simulation. For example, 3BR rates are included in the simulations, as 3BR contributes as an electron heating effect. If the 3BR rates in the plasma differ from the traditionally accepted Mansbach and Keck rates [1], then the electron temperatures predicted by the simulation will be incorrect. This technique does not, then, alleviate the need for a direct measurement of electron temperatures, particularly given several of the open questions regarding electron behavior and electron-ion interactions in these systems.

2.3.4 Using Plasma Characteristics

Previous work had used the cold plasma resonance to determine the time-dependent average density of the UCP by exploiting the density dependence of the cold plasma resonance $\omega_p^2(r) = \frac{n_e(r)e^2}{\epsilon_0 m_e}$ [7, 34]. A low-power RF field excites the plasma resonance to determine when in the plasma expansion the average density corresponds to the ω of the applied field. An effect that was noticed at that time, but not explored, was that an applied RF field at a particular frequency could drive an electron resonance at more than one time (or, equivalently, at more than one av-

erage density), giving multiple peaks in the time-dependent electron emission signal, provided the applied RF field was above some moderately low-power threshold.

Careful observation of these additional resonances indicated that, rather than exciting just the cold plasma resonance, an applied RF field would excite a series of resonances that we identified as Tonks-Dattner (TD) resonances [35, 36]. These TD resonances arise from finite-temperature extensions of the cold plasma resonance in an inhomogeneous finite-sized plasma obeying the Bohm-Gross dispersion relationship. Recalling the cold plasma resonant frequency:

$$\omega_p^2(r) = \frac{n_e(r)e^2}{\epsilon_0 m_e} \tag{2.2}$$

the applicable dispersion relationship for a finite electron temperature takes the form [37]:

$$\omega_i^2 = \omega_p^2(r) + \frac{3k_B T_e}{m_e} k_i^2(r) \tag{2.3}$$

where $k(r)$ is the local wave number and $\omega_p(r)$ is the local plasma frequency, assuming a local density approximation. Thus as $k \to 0$, the wave has frequency ω_p, and high k results in a linearly dispersive wave (that is, an electron acoustic wave) in the plasma.

Physically, these TD resonances are simply standing acoustic waves in the electron system with frequencies determined by the dispersion relationship of Eq. 2.3. The inner turning point for the standing wave is the radial distance r_c where the local plasma frequency $\omega_p(r)$ is equal to the frequency of the standing TD wave; at radii less than this point, the plasma frequency is greater than the TD wave frequency, so the wave cannot propagate into the core of the plasma and is

evanescent in this region. The outer turning point r_w is not as clearly defined as r_c and is addressed in greater detail in the following paragraphs. Using this concept of a standing wave, and adapting the work of [38] for application to a spherical system (resulting in the expression $\bigtriangledown^2\delta n(r) + k^2(r)\delta n(r) = 0$ for the density fluctuation $\delta n(r)$), one can simply find the WKB solution for the wave:

$$\mathrm{Tan}\Big(\int_{r_c}^{r_w} k(r)\ dr\Big) = \frac{r_w}{2}(k(r_w)), \omega_p(0) < \omega \tag{2.4}$$

$$\int_{r_c}^{r_w} k(r)\ dr = (i + \frac{1}{4})\pi, i = 1, 2, 3, \cdots, \omega_p(0) > \omega$$

where $\omega_p(0)$ corresponds to the peak plasma density.

Since $k^2(r) = [\omega_i^2 - \omega_p^2(r)]/(3k_BT_e/m_e)$, we can numerically solve Equations 2.4 to determine the resonant frequency ω_i. We assume a spherically symmetric Gaussian density distribution with self-similar expansion (per Eq. 1.2). As mentioned above, r_c is the well-defined inner turning point for the TD standing waves ($\omega_p(r_c) = \omega_i$). The outer turning point, designated r_w (since previous laboratory observations of these resonances were done in cylinders with well-defined walls), is a free parameter in our solutions, as the assumed density distribution of Eq. 1.2 provides no obvious outer turning point for the electron waves.

We measured these resonances in our plasma by creating the UCP while applying RF fields of varying frequencies to the plasma. The RF fields were coupled onto the grid immediately above the plasma (the top grid in Fig. 1.7). The plasma then expands in the RF field and, as its average density drops such that its resonant frequencies pass through the frequency of the applied RF field, electron resonances are excited by the field and a burst of additional electrons are emitted from the

plasma. Examples of the resulting time-dependent electron emission signals are shown in Fig. 2.3. The electron peaks are clearly visible in the first 40 μs of plasma expansion. We subtract a background curve (an electron emission signal without any applied RF) from these curves, fit each resonance peak to a Gaussian, and use the centerpoint of that Gaussian as an estimate for the time at which the peak occurs. Note that the distortion of the curves with higher-frequency RF fields makes the background subtraction less effective; however, this distortion is minimized by using as little RF power as possible while still exciting several resonance modes. The results, after this was repeated for several different RF frequencies, are plotted in Fig. 2.4.

The RF is on for the entire duration of the plasma expansion; to verify the multiple observed peaks are not simply ringing features, we applied RF in a short 1 μs pulse and stepped the pulse through the plasma. Combining the electron emission signals resulting from the stepped pulse and comparing that composite signal to the signal obtained by a constantly applied RF field, we observed that the two traces showed the same multiple peak features, verifying that the observed peaks correspond to excitation of plasma modes.

The times at which electron resonances occur are roughly independent of the power of the RF field applied (although very high RF power can distort the signal and affect the times at which later peaks occur). However, it should be noted that whether the resonances occur or not was seen to be a function of the RF power; as the RF frequency increases, more power in the field is required to excite the resonances to the point where electrons are ejected (as in Figure 2.3). This may

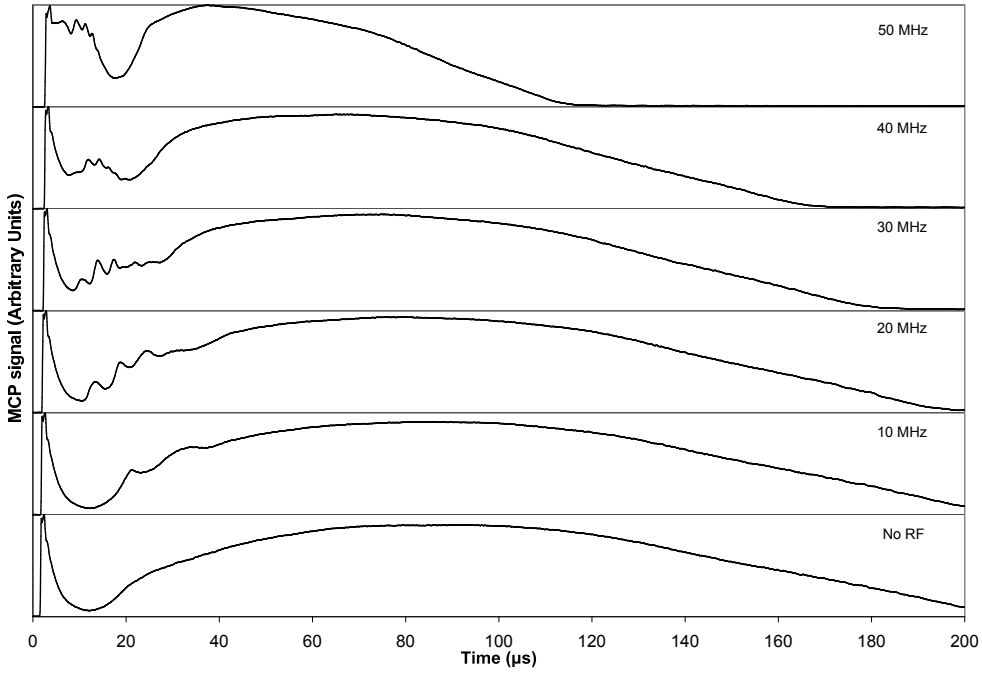

Figure 2.3: Examples of electron emission curves with Tonks-Dattner excitations due to external applied RF fields. Note that at differing RF frequencies, the times (and thus densities) at which the electron resonances occur differ.

account for the degree to which the plasma is distorted when higher RF frequencies are applied; because of the power with which the RF field is driving the resonances, the plasma electron system is likely heated and undergoes an increased rate of electron evaporation, shortening the lifetime of the plasma. Therefore, for any given RF frequency applied to the plasma, we set the power in the RF field to be the minimum power at which the electron resonance features are clearly observable in the electron emission signal. This RF power typically ranges from about -45 dBm to -5 dBm at the vacuum chamber feedthrough (with estimated field amplitudes at the plasma of about 0.4-50 mV/cm), with higher frequencies requiring more power. Furthermore, we typically average each signal over 40 to 60 experimental cycles, in order to improve our signal-to-noise resolution.

After several sets of such measurements, the times at which electron resonances occur are recorded (using the Gaussian fits to the observed electron emission peaks) and plotted as a function of the applied RF field frequency [39] (see Fig. 2.4). While the first (leftmost) curve is simply the cold resonance curve and is thus easily modeled using Eq. 2.2, the remaining curves together make up the Tonks-Dattner resonance curves described by the discrete modes of the dispersion relation of Eq. 2.3. In order to use these resonance curves to determine the electron temperature, we must fit the WKB solutions (Eq. 2.4) to the observed resonance curves of Fig. 2.4. The first step in this process is approximating the plasma expansion with the expression of Eq. 1.2, which is particularly valid for this application because we are only concerned with the first 40 μs of the plasma lifetime, over which time only a small percentage of the electrons have been lost to evaporation. By fitting the

first measured curve (the cold plasma resonance curve) of Fig. 2.4 using Eq. 2.2 together with a time-dependent spatially averaged density as a function of time (calculated with Eq. 1.2), we determine various plasma parameters (such as initial peak density $n(0,0)$ and asymptotic expansion velocity v) to about 10-20% accuracy for any particular set of experimental data; we note that the parameters determined with this fit are consistent with measurements made using other techniques, such as absorption imaging.

Thus, using the cold plasma resonance curve as a calibration tool for several plasma parameters, we consider the TD resonance curves. We determine ω_p^2 as a function of time using the cold plasma resonance curve and, using the outer turning point r_w as a free fitting parameter, numerically solve for the wave number k in Eq. 2.4. Thus, having determined ω_p^2 and k for the TD resonances, as well as knowing the TD frequency ω_i^2 (determined by the frequency of the applied RF fields), the electron temperature in Eq. 2.3 is clearly defined as a function of time (remembering the time dependence is contained in both the k and ω_p terms). The resulting time-dependent electron temperature measurements are given in Figure 2.5, and the fits to our measured data using the estimated electron temperatures and our best-fit r_w are plotted as solid lines in Figure 2.4.

At this point, the outer turning point r_w should be addressed in more detail. This turning point is clearly a potentially important parameter for this fit process; indeed, varying it a modest amount (10%) has a strong impact on the resulting temperature estimates (20%). However, after fitting to the measured TD resonance curves, the required turning point r_w is approximately $3.2\sigma(t)$ (where $\sigma(t)$ is the

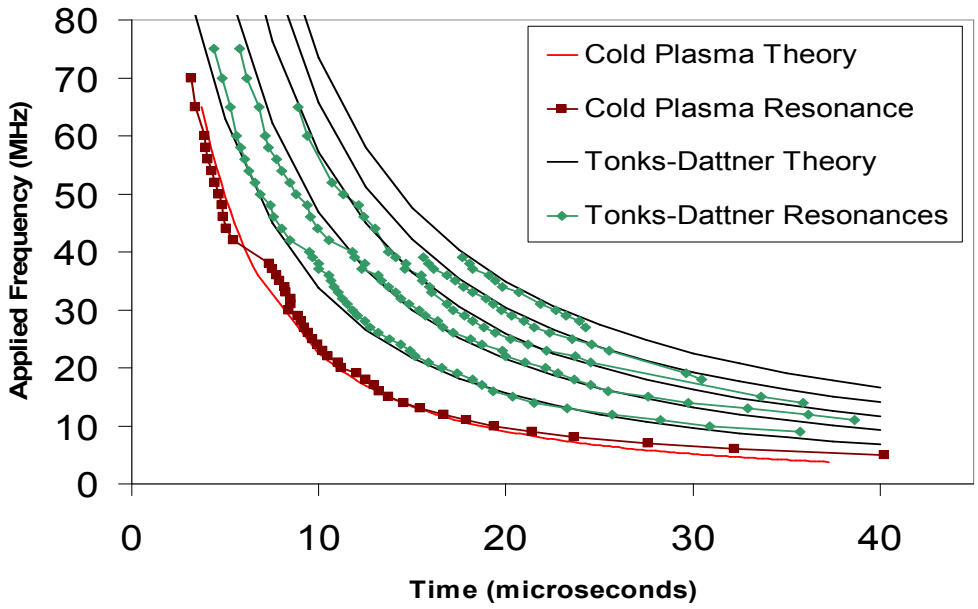

Figure 2.4: A plot of the applied frequencies vs. the times at which electron resonances are observed. The first (leftmost) curve is simply the cold plasma resonance and is thus a direct measurement of the average density of the UCP as a function of time; it has fit parameters of $n_e(0) = 1.9 \times 10^9$ cm^{-3} and $v = 65$ m/s. The other curves together make up the Tonks-Dattner resonance curves. From [39].

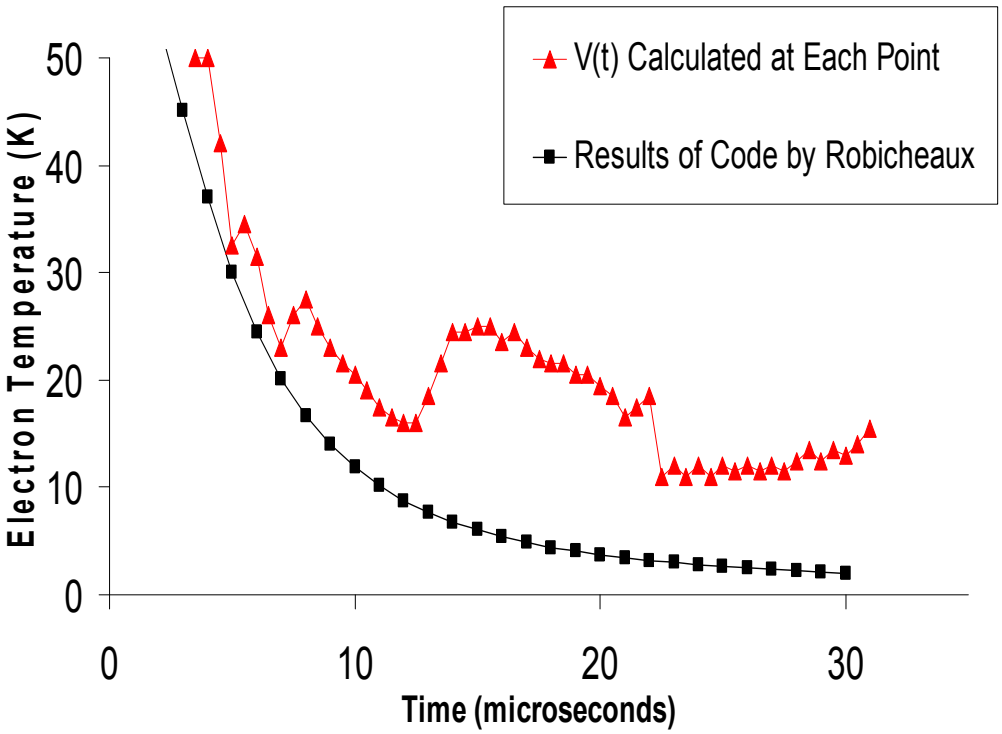

Figure 2.5: The electron temperatures, as determined by using Tonks-Dattner resonances. Also plotted is the predicted electron temperatures, from a simulation by Francis Robicheaux [40].

time-dependent 1-σ point of the plasma, as in Eq. 1.2). This is very close to the location of an ion shock wave predicted in simulations [9]. Such an ion density spike would be able to act as a turning point for a standing electron wave; however, damping effects not included in that simulation may serve to smooth out the shock wave, so that the simulation's prediction is by no means firm. It is also difficult to experimentally verify, as the predicted ion density spike is a relatively minor perturbation in the low-density region of the plasma and no currently available techniques (in any of the UCP systems) are expected to resolve such a feature. Another explanation for the outer turning point is that our fitted r_w is very close to the point in the plasma where the Debye length $\lambda(r,t) \sim \sigma(t)$; that is, the local Debye length at the $3\sigma(t)$ radius is approximately $1\sigma(t)$. Thus, near r_w, the system makes the transition from a plasma (where the Debye length is less than the system size) to a charged gas and this transition region may serve to strongly damp the TD wave, providing an outer turning point.

As is indicated in the estimated electron temperatures (Fig. 2.5), temperatures measured in this manner are similar to the simulation results of Francis Robicheaux [40]. There is clearly a possible problem at certain times (note the odd plateau-like feature around 15-20 μs); this is probably a direct result of the cold plasma resonance measurements (see Fig. 2.4 at 15-20 μs). The reason for the clear bulge in the resonance curves for applied frequencies around 30-40 MHz is not completely understood; we see no evidence of an electrical resonance in our system at those frequencies, nor does the feature appear to be a simple error, as it is very repeatable. The most likely explanation is that, at those frequencies, the excited plasma

resonances occur at such a time in the plasma expansion that the plasma signal is strongly distorted in such a way as to systematically skew the measured times at which the resonances occur (see Fig. 2.3, for higher applied frequencies). Most likely, the correct temperature measurements would smoothly connect between t$\sim$12 and t$\sim$22 μs.

An additional point to note in Figure 2.5 is the slight upward trend in the calculated electron temperatures at times greater than about 25 μs. This highlights a general possible weakness in the use of these mode frequencies to determine electron temperatures. Looking at Fig. 2.4, it is clear that the fitted theory curves deviate from our resonance measurements at such late times. Since the fitted theory curves are the basis for the electron temperature measurements, such a systematic deviation from measured resonances will result in a clearly erroneous temperature measurement. This weakness, however, can be compensated for by restricting the theory fit to times for which the fit is close to the resonance measurements. Alternatively, our fits assume an r_w that is constant with respect to $\sigma(t)$ ($\sim 3.2\sigma(t)$); instead, it is possible the r_w can change as the plasma expands, and proper treatment of this could improve these fits. Of course, associated with this problem is the overall sensitivity of the extracted temperature measurements to the r_w used.

A problem with this technique is the difficulty of applying it to plasmas with low initial electron energies. When initial electron temperatures (the initial T_e as set by the energy of the green photon in the photoionization process) are less than about 30 K, the resonance curves as shown in Fig. 2.4 do not yield sufficiently good fits to Eq. 2.4 to provide reasonable electron temperature curves. The reason for

this is currently not understood; although the Tonks-Dattner resonances are still visible in these lower-energy plasmas, there is no obvious reason why Eq. 2.3 should not apply such that Eq. 2.4 are no longer adequate fits to the data.

In summary, this was the first measurement of collective electron modes in ultracold plasmas. As a result of the Tonks-Dattner resonance theory, we developed a technique that allows for late-time (up to $\sim$ 35 μs) measurements of electron temperatures in ultracold plasmas. There are three issues with this technique that lessen its effectiveness. First, the lack of firm knowledge regarding the outer turning point r_w of the standing Tonks-Dattner wave introduces an added fit parameter that will obviously hinder the fit of the parameter of interest (the electron temperatures), particularly given the sensitivity of these fits to the position of r_w. While there is some theoretical evidence for an ion shock wave at the location our fits choose for the outer turning point, solid experimental evidence for such a density feature would clearly be preferable, although a full theoretical treatment of TD resonances in our system (without assumptions regarding the outer turning point r_w) would obviously be of great value. Second, the fits to the Tonks-Dattner curves must be done carefully and only over the range for which the TD expressions provide a good fit to the TD curves. Otherwise, the fits may imply physically unreasonable temperature changes, although there is always a danger in only including data that fits well to the theory. Third, this technique is limited to plasmas with fairly high initial temperatures. This limitation is linked to the second limitation, of course, as both are restrictions based on parameters for which the TD theory adequately fits the measured resonance data. At this point, using Tonks-Dattner resonances as a

means to measure the electron temperatures is still somewhat problematic. However, in principle it should prove to be a very effective technique, particularly as some of the problematic aspects are studied in greater detail and a better theoretical approach, more sophisticated than relying on a simple WKB approximation which can adequately treat the lack of a well-defined outer turning point r_w, is developed.

2.3.5 Using Collision Rates

We are currently exploring the use of the temperature dependencies of low-temperature collisions in UCPs as a means to measure the electron temperatures. Similar to the previous technique, it is possible to measure various electron temperature dependent rates in the plasma (as opposed to macroscopic collective modes of plasmas) to estimate electron temperatures. In particular, if one accepts the typical three-body recombination rates (such as in [1]), a measurement of the 3BR rate could then be used in an inverted rate expression to extract electron temperatures [41]. This approach is actually quite promising, as the strong $T_e^{-4.5}$ dependence of the rate on electron temperature will tend to suppress errors in the rate measurement (as T_e will have a -2/9 dependence on the measured rates), allowing for very well determined electron temperature measurements. This approach will be addressed in detail in Chapter 4.

Chapter 3

Rydberg Atoms in Ultracold Plasmas

3.1 Overview

Rydberg atoms, neutral atoms with a high (N> ∼15) principal quantum number, are an important component in ultracold plasmas; they are formed in plasmas by recombination collisions. A great deal of work has been done exploring the similarities between a cold, dense Rydberg gas and a UCP, as well as the manner in which one might transition into the other [18, 19, 20, 21, 22]. These similarities are due to the very nature of a Rydberg atom; because Rydberg atoms are highly excited and are thus weakly bound, they are easily ionized in a Rydberg gas by Rydberg-Rydberg collisions and a resulting cascade of Rydberg-electron collisions (forming a plasma), as well as easily formed in a plasma (via three-body recombination). In this manner, energy can be pumped into a UCP as Rydberg atoms are formed, as three-body recombination is a heating process for the electron system.

Another aspect of Rydbergs in a UCP is that they will be spread out in a tremendous number of states, both in N and l. For example, in xenon the neutral atom population can be distributed from a minimum of N=6 (the ground state) up to roughly $\mathrm{N}_{max} = \sqrt{13.6\mathrm{eV}/2k_bT_e}$ ∼85 for T_e=10K (the so-called thermal cutoff, other cutoffs are discussed in [42]), with full l-sublevel mixing (due to the highly collisional nature of the system). Additionally, the Rydberg distribution is not static,

but instead is predicted to be in a slowly-changing equilibrium distribution [9, 28] due to the differing density, temperature, and N-level dependencies of three-body recombination, electron-Rydberg scattering, radiative decay, and blackbody-induced transitions.

The Rydberg atom population in a UCP is thus of extraordinary interest, due to the importance of Rydbergs in affecting the behavior of the UCP. Of even greater interest, however, is the experimental verification of three-body recombination rates at low temperatures. Several theorists predict a correction to the classic Mansbach and Keck 3BR rates [1] (a seminal work on 3BR from 1969) must be made to describe recombination at UCP electron temperatures, which is of obvious importance to experiments such as the creation of anti-hydrogen using ultracold antiparticle plasmas [23, 24]. Such anti-hydrogen creation is explicitly dependent on three-body recombination as a production mechanism.

3.2 Rydberg Processes

Several Rydberg processes are of interest in ultracold plasmas. There are the processes by which Rydbergs are created - three-body recombination (3BR), dielectric recombination (DR), and radiative recombination (RR). Rydbergs can shift energy levels by electron-Rydberg collisions (ERCu, ERCd for upshifting and downshifting the N level, respectively), radiative decay (RD), and blackbody-induced transitions (BB). Rydbergs can be ionized by level up-shifting processes, namely ERCu and BB.

3.2.1 Rydberg Creation

3.2.1.1 Three-Body Recombination

Three-body recombination, a particle loss process for a plasma ($e^- + e^- + A^+ \rightarrow e^- + A^*$), is the dominant process by which Rybergs can be created in UCPs, due to the low electron temperatures. The most commonly used expression for 3BR is from the Monte Carlo work of Mansbach and Keck [1]. Integrating over the plasma ions gives the number of recombinations per second in the entire plasma:

$$R_{3BR}\,(s^{-1}) = K_{3BR}\,T_e^{-9/2} \int n_e^2(r) n_i(r) 4\pi r^2 dr \tag{3.1}$$

or equivalently (using eV with the introduction of N_{max})

$$R_{3BR}\,(s^{-1}) = \frac{1\mathrm{eV}}{k_B T_e} \mathrm{N}_{max}^7 2.8 \times 10^{-42} \frac{\mathrm{m}^6}{\mathrm{s}} \int n_e^2(r) n_i(r) 4\pi r^2 dr, \tag{3.2}$$

where n_e and n_i are the electron and ion spatial density distributions, respectively, $K_{3\mathrm{BR}} = 4.5 \times 10^{-21}\ \mathrm{m}^6\mathrm{K}^{9/2}\mathrm{s}^{-1}$, and $\mathrm{N}_{max} = \sqrt{13.6\mathrm{eV}/2k_B T_e}$. Note that work subsequent to [1] results in $K_{3\mathrm{BR}}$ values that can differ [43]. The second form of the equation is from [9] and is a useful visualization of the manner in which the electron temperature contributes to the rate expression.

The formal derivation of Eq. 3.1 can be found in various references [1, 42, 44]; these derivations either use Monte Carlo code with classical trajectories to model recombination or they begin with empirical expressions for the collisional ionization processes, then use detailed balance to determine the appropriate form for the rate of 3BR. More interesting, however, is the manner in which the unusual -9/2 exponent on T_e comes about. As discussed in [45], given the electron-ion seperation of $b =$

e^2/k_BT_e (that is, the Thompson radius), the frequency of an electron-ion collision is roughly $n_e b^2 v_e$, where n_e and v_e are the electron density and average velocity. The probability of a second electron being in the volume close enough to take part in this collision is proportional to $n_e b^3$. The three-body recombination rate is just this probability times the frequency of ion-electron collisions, which is proportional to $n_e^2 b^5 v_e$; as $b \sim T_e^{-1}$ and $v_e \sim T_e^{-1/2}$, the 3BR rate clearly has a dependence on electron temperature that goes as $T_e^{-9/2}$. Likewise, the dependence on n_e^2 is easily demonstrated in this manner; Eq. 3.1 and 3.2 have the additional n_i dependence because both equations are integrated over the ion distribution to give a total 3BR rate in the plasma (as opposed to the rate for one ion alone).

The significance of N_{max} is that it is the electron-temperature-dependent maximum Rydberg level that can be formed in the plasma. This is simply because higher N-levels are too close to the ionization threshold for the electron energies in the plasma, such that the binding energies of the higher N-levels are less than typical energies of the plasma electrons, making a successful recombination event highly unlikely. Three-body recombination forms Rydbergs with a population distribution that goes as N^6 up to the N_{max}, where the distribution is approximated with a truncation (see Fig. 3.1); this is the origin of the N_{max}^7 term in Eq. 3.2, as that equation is essentially the integral of the plotted 3BR population distribution.

Given the very strong inverse electron temperature dependence in Eq. 3.1, this process is clearly of great importance in UCP systems. Several theoretical works [42, 46] , as well as some experimental measurements [47, 48], seem to indicate that

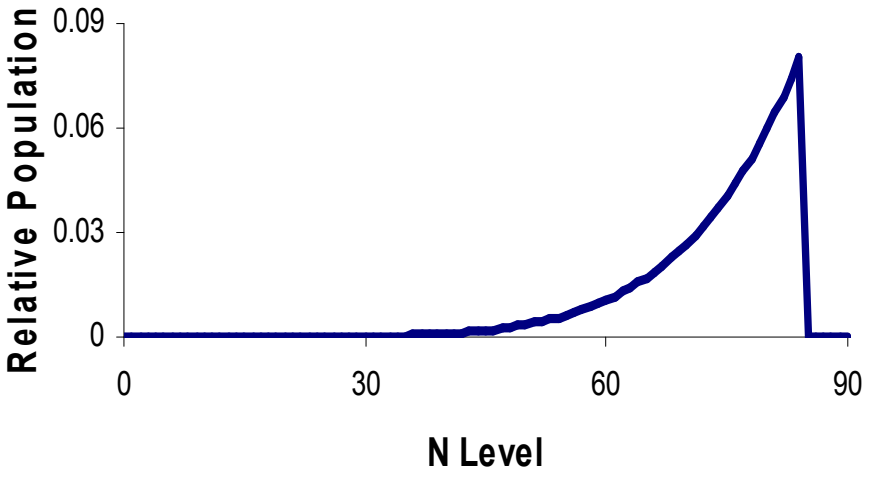

Figure 3.1: The predicted relative population distribution of Rydberg atoms due to three-body recombination for a plasma with T_e=10 K, resulting in a cutoff N_{max}=85. This distribution scales as N^6.

Eq. 3.1 must be altered to account for low-temperature dynamics. The three-body recombination process, as well as techniques to measure it in ultracold plasmas, will be addressed in greater detail in the following chapter.

Note that 3BR is a process that clearly heats the electron system in the plasma (due to the energy released by the recombination of an ion and electron being carried from the collision by the extra electron), yet has a higher rate of occurrence for a colder plasma. This leads to the possibility of a thermostat effect in the UCP; as temperatures drop due to various processes (and particularly driven by equilibration with the ions and by adiabatic expansion), 3BR turns on and arrests the decline in temperature. Thus 3BR is a critical process in determining the time-dependent temperature of UCPs.

3.2.1.2 Radiative Recombination

Radiative recombination, whereby a Rydberg atom is formed through an electron-ion collision with a released photon ($e^- + A^+ \rightarrow \gamma + A^*$) [49], scales much less strongly with inverse temperature than 3BR:

$$R_{RR}\,(s^{-1}) = K_{RR}\,(k_B T_e)^{-1/2} \int n_e(r) n_i(r) 4\pi r^2 dr, \tag{3.3}$$

where $K_{\mathrm{RR}} = 2.7 \times 10^{-19}\mathrm{m}^3\mathrm{eVs}^{-1}$. As a result, it clearly contributes substantially less to Rydberg formation rates at UCP temperatures and densities than 3BR. It is therefore neglected in this work; as an example of the difference in the rates, for $n_e = n_i$ defined by Eq. 1.2 with $n(0,0) = 2 \times 10^{15}$ m^{-3}, $\sigma_0 = 280$ μm, and t=0, and

assuming $T_e = 10$ K, the radiative recombination rate using Eq. 3.3 is 4.5×10^3 s^{-1}, while the 3BR rate using Eq. 3.1 or 3.2 is 7.55×10^{10} s^{-1}.

3.2.1.3 Dielectric Recombination

Dielectric recombination ($e^- + A^+ \leftrightarrow A^{**} \rightarrow \gamma + A^*$) [50] is very similar to radiative recombination, but an intermediate state is briefly occupied before photon emission. Because DR has a similar T_e and n_e dependence as RR, DR is much less important than 3BR for Rydberg formation in a UCP and is thus neglected. Research on the particular rates of this process is ongoing in other systems, but DR appears to be only significant (or even comparable to RR) at electron densities and temperatures many orders of magnitude greater than those in our system.

3.2.2 Rydberg Energy-Shifting Processes

3.2.2.1 Electron-Rydberg Collisions

Perhaps the most dominant process in a plasma by which Rydbergs can change bound energy levels is electron-Rydberg collisions (ERC) ($e^- + A^*(\mathrm{N}, l) \rightarrow e^- + A^*(\mathrm{N'}, l')$). Such collisions can either up-shift (ERCu) or down-shift (ERCd) the principal quantum number N of the Rydberg atom.

The total excitation rate for a given Rydberg atom with binding energy E_r and principal quantum number $N = \sqrt{13.6eV/E_r}$ takes the form:

$$R_{ERCu}\,(s^{-1}) = 55 n_e(r) \left(\frac{k_B T_e}{27.2\mathrm{eV}}\right)^{0.83} \mathrm{N}^{4.66} a_0^2 \alpha c, \tag{3.4}$$

and de-excitation:

$$R_{ERCd}\,(s^{-1}) = 7.2 n_e(r) \left(\frac{27.2\text{eV}}{k_B T_e}\right)^{0.17} \text{N}^{2.66} a_0^2 \alpha c, \tag{3.5}$$

where n_e is the electron density, α is the fine structure constant, and a_0 is the Bohr radius [1, 9, 51]; these rates, like the 3BR rates, are largely the result of work by Mansbach and Keck and the use of detailed balance for rates in equilibrium with the Thompson radius as a characteristic interaction length. The total rate of occurance of any electron-Rydberg collision is simply the sum of R_{ERCu} and R_{ERCd}. Note that when the binding energy $\text{E}_r = 3.83 k_B T_e$ with the corresponding N-level designated $\text{N}_= = \sqrt{3.55\text{eV}/k_B T_e}$, the probability of ERCu is equal to the probability of ERCd. For N>$\text{N}_=$, Rydbergs are much more likely to be upshifted in N than downshifted by electron-Rydberg collisions, such that they will strongly tend toward a cascade-like excitation to ionization. Similarly, for N<$\text{N}_=$, Rydbergs will have a slight tendency to be de-excited via collisions with electrons; however, in this regime the two rates are much more similar than for when N>$\text{N}_=$, resulting in much less of a likelihood of a collisionally-induced cascade to low N-levels. Note that this means high N Rydbergs will overall provide a heat sink for the UCP electron system, while low N Rydbergs will provide a smaller (on a per-Rydberg basis) heat source. Refer to Fig 3.2 for examples of the N-dependent rates.

Assembling simple steady-state Monte Carlo rate code for ERCu and ERCd rates for UCP parameters, it is clear that the electron-Rydberg collision process will result in very characteristic Rydberg spectra (Fig. 3.3). That is, Rydberg levels

greater than $N_=$ will tend to be depleted, while population will accumulate in the levels less than $N_=$.

3.2.2.2 Radiative Decay

Like any excited atom, Rydberg atoms can emit a photon and relax into a lower energy state via radiative decay. The rate from an l-averaged initial manifold N_i to a similarly averaged final manifold N_f is [9]:

$$R_{RD:N_i \to N_f}\,(s^{-1}) = \frac{8\alpha^4 c}{3\sqrt{3}\pi a_0}\frac{1}{\nu_i^5 \nu_f}\frac{1}{1-\nu_i^2/\nu_f^2} \tag{3.6}$$

where the total rate of a particular N_i radiatively decaying to any final state is simply the sum of the R_{RD} expressions for N_f=6 to N_f=N_i-1. Note that this is averaged over the l sublevels, which is valid in our plasma given the collisional level mixing that occurs; in the low- and high-l level limits, the lifetimes of individual l-levels have the form $\tau_{rad}(l=0) \propto n^3$ and $\tau_{rad}(l=n) \propto n^5$ [52]. This process is of greater importance for lower N-levels. Note that this tends to heat the plasma (or, more correctly, removes a possible cooling mechanism), as a decay in the N level results in a decreased chance for the Rydberg to then undergo an excitation due to a electron-Rydberg collision event (ERCu).

3.2.2.3 Blackbody Driven Transitions

Noting that a blackbody driven transition is simply a stimulated emission/absorption process (as compared to the spontaneous emission of radia-

tive decay; Eq. 3.6 is effectively just the expression for the relevant Einstein A coefficients), one can simply derive the rate of BB by adding to the RD expression the term to describe the mean number of photons excited in the field mode at the blackbody temperature T_{BB} [52]:

$$R_{BB:N_i \to N_f}\left(s^{-1}\right) = R_{RD:N_i \to N_f} \times 1/\left(e^{\frac{\hbar\nu}{k_B T_{BB}}} - 1\right) \tag{3.7}$$

The overall effect of blackbody-driven transitions alone is relatively minor, as it can drive both up- and down-shifting transitions with similar rates. However, because of this diffusion effect, combined with other level-shifting processes that more heavily favor either up- or down-shifting of the Rydberg atom binding energies, BB transitions can influence the Rydberg spectra by effectively starting a cascade-like chain of transitions.

3.2.2.4 Combined Effects of Level-Shifting Processes

With such a variety of processes available by which Rydberg atoms can change energy levels, it is not immediately clear what type of Rydberg population distribution should result. We wrote Monte Carlo rate code for this purpose - at this point, three-body recombination is not included. Starting with Rydberg atoms randomly distributed (with a spherical Gaussian distribution) in radial location in the plasma and a flat distribution in principal quantum numbers from N=6 to N=200, the probability of a level-shifting process occurring for each Rydberg is determined for a particular time step. Each Rydberg is then assigned its new energy level, and the process is repeated. Initially the level distributions are similar to the artificial

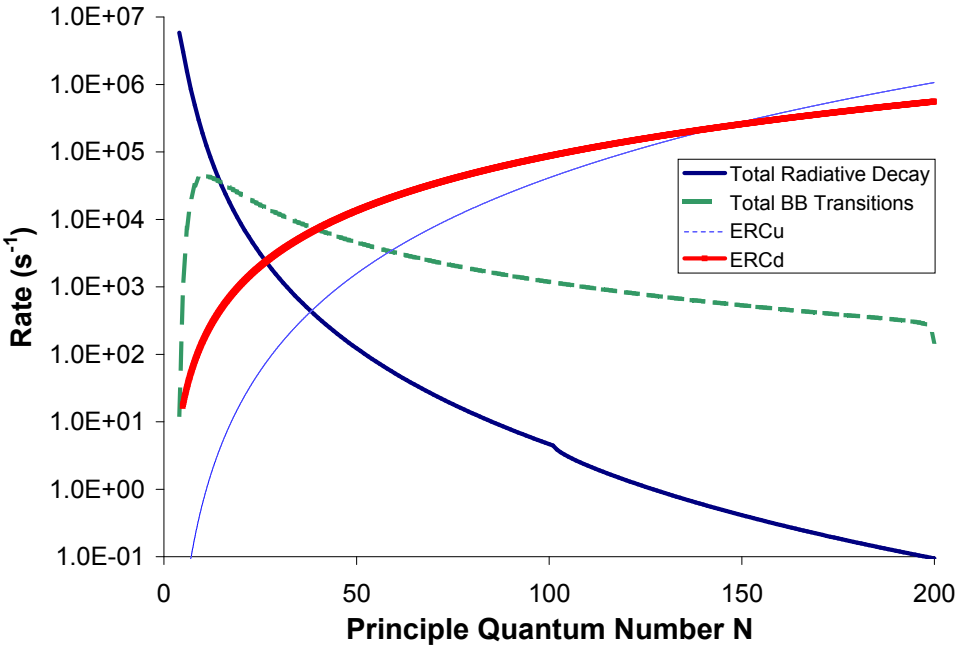

Figure 3.2: Estimates of various level-shifting rates for Rydbergs in a plasma. Radiative decay and blackbody transitions are independent of plasma parameters. The electron-Rydberg collision curves are for an electron system at 2 K and a density of 1.25×10^6 cm^{-3} (roughly plasma parameters at the center of the plasma after 50 μs of expansion). Note that the blackbody transition curve is the sum of both up- and down-shifting BB transitions; however, the rates for up- and down-shifting BB transitions are roughly equal.

flat initial distribution; however, within about 1 μs (using 100 ns timesteps), the distribution reaches a near-steady-state (noting that at this point, there is no Rydberg source in the code, so that eventually the distributions should reduce to simply accumulating population in the ground level and in the topmost, 'ionized' level). This rate code is very similar to the work described in [9], although more limited in scope, as our interest was not in a full plasma simulation, but was instead focused on the Rydberg population evolution over short times.

The final quasi-steady-state distribution of Rydberg levels is somewhat independent of the initial distribution; that is, given a particular electron temperature, there is a particular shape to the population distribution that can result. Rydbergs that are initially in states that are too high or too low for the quasi-equilibrium distribution quickly (within a couple of timesteps) ionize or relax to the ground state, while those occupying levels that are favored by the steady-state distribution are lost from the system much more slowly. Thus varying the initial distribution (either in relative distribution or in total number of Rydbergs used) typically only has a multiplicative scaling effect on the final distribution. One option that we sometimes use is to run the code several times sequentially while taking the output of each step, renormalizing it, and using it as the initial distribution for the next iteration.

Ignoring any atoms in the N<6 or N=200 states, example results are plotted in Fig. 3.3. These results are for a plasma with an initial peak density of 2×10^9 cm^{-3}, initial size σ = 280 μm, an asymptotic velocity of v=65 m/s, electron temperature T_e = 2 K, and after 50 μs of plasma expansion (such that the peak density $n_0(t = 50\mu\text{s}) = 1.25 \times 10^6$ m^{-3} and $\sigma(t = 50\mu\text{s}) = 3.25$ mm). Of note is the higher-N

dropoff in population due to dominance of the ERCu process for N>144 (recall Fig. 3.2). Also, at low N, the effects of radiative decay become quite obvious.

The addition of three-body recombination as a possible rate in the Monte Carlo simulation provides a source for new Rydberg formation at each time step. Since three-body recombination tends to form Rydbergs in higher-N states, the result is a population distribution that differs from Figure 3.3 at higher N. As the Monte Carlo code we have written is not a comprehensive simulation of the plasma, but is instead a means to gain some idea of the relative populations at specific times in the plasma, adding 3BR to the Rydberg rates must be done with care. The simulation must now track two different populations of Rydberg atoms - the first population (a scalable population), consisting of a group of Rydbergs in an initial distribution and reflecting the number of Rydbergs we expect in the plasma at the start of the simulation, is free to change its distribution as the simulation progresses (as discussed earlier). The second population is due to Rydbergs that are created by 3BR as the simulation proceeds, and are then free to change N-levels following the same rate equations as the initial scalable population follows. This distinction between populations is important - as noted earlier, the N-level distribution of Rydbergs at the start of the simulation is not well understood and must be estimated, resulting in a multiplicatively uncertain distribution (i.e., it is scalable if we know how many Rydbergs should be present at the start of the simulation). However, the Rydbergs that form by 3BR should not have a multiplicatively scalable distribution, as the number formed by this process is well defined, given the plasma parameters the simulation uses and the 3BR rate expression.

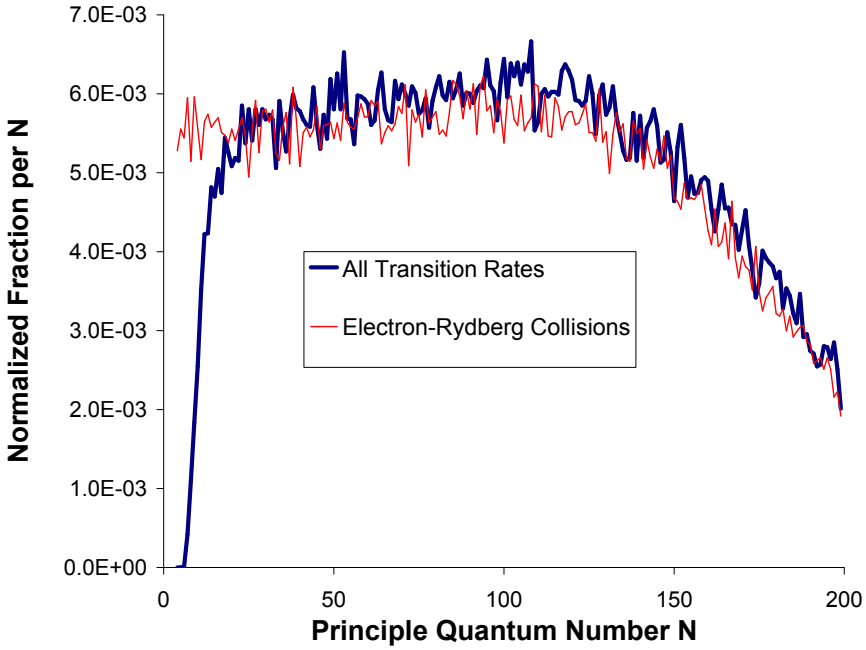

Figure 3.3: Relative population distributions of Rydberg atoms subjected to only electron-Rydberg collisions (red, thin line) and subjected to electron-Rydberg collisions together with blackbody-induced transitions and radiative decay (blue, heavy line). Note that at higher N, the population is relatively depleted due to the high rate of up-shifting electron-Rydberg collisions. At low N, the population is depleted due to the effects of radiative decay. Blackbody-induced transitions play a relatively minor role in this Monte Carlo rate code.

Keeping this in mind, when 3BR is included in the Monte Carlo code, the initial distribution of Rydberg atoms is created and is allowed to change distributions as previously discussed. Separate from this, at each time step the number of Rydbergs produced by 3BR is calculated; they are then randomly assigned radial locations in the plasma (weighted by density) and randomly given an initial N-level based on the N^6 distribution of Fig. 3.1. These new Rydbergs are then allowed to change N-level in the same manner as the Rydbergs in the initial distribution.

At the end of the simulation, the two populations can be added together in a weighted manner so that the total population correctly reflects the number of Rydbergs expected (or measured) in the plasma; see Fig. 3.4, where the code was run with 3BR included and scaled afterwards to obtain a distribution for a plasma with an expected number of Rydbergs equal to about 6×10^3.

3.2.3 Rydberg Ionization in the Plasma

As mentioned previously, several of the Rydberg processes in a UCP can change the binding energies of the Rydberg atoms. Once a Rydberg is weakly bound and near $N_{max} \sim \sqrt{13.6\text{eV}/2k_BT_e}$, it can then easily be ionized by a single electron-Rydberg collision. Thus, Rydberg levels above $N_=$ will be depleted in population, as in that range of binding energies, processes that will increase the N-level are favored over those that will decrease the principal quantum number such that Rydberg atoms in this range of N-levels are prone to ionization.

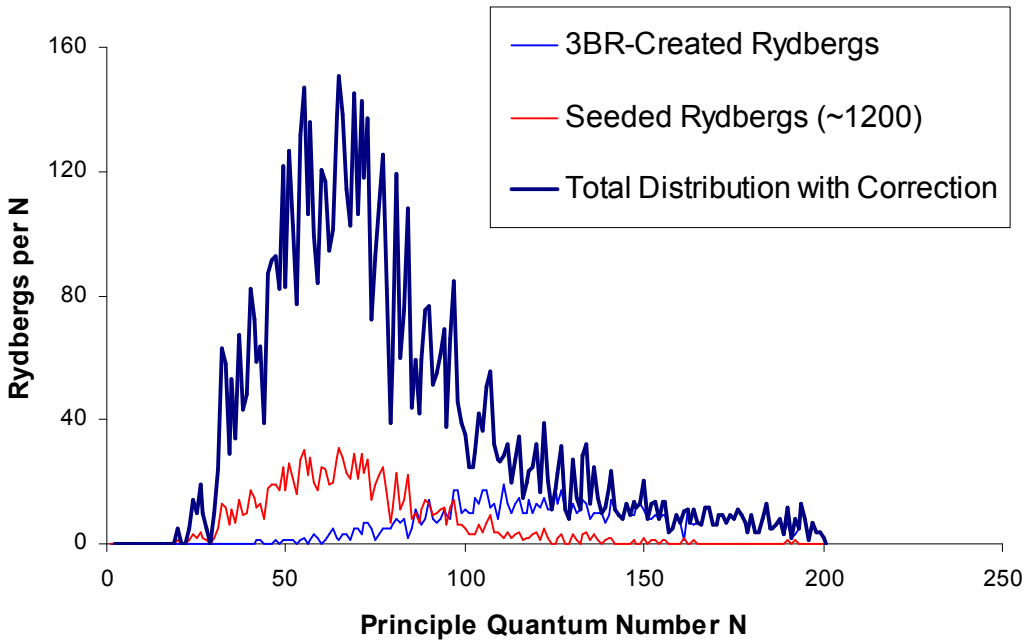

Figure 3.4: Results from the Monte Carlo rate code for Rydberg atom population distributions. The thin blue line (low amplitude and centered at lower N) is similar to the heavy blue curve of Figure 3.3; this is the population distribution of an initial group of Rydbergs and contains about 1.2×10^3 Rydberg atoms. The thin red line (low amplitude and centered at higher N) is the distribution that results from 3BR-created Rydbergs which, after creation, are allowed to shift N-level by the various mechanisms previously discussed. The heavy blue line is the weighted sum of the two distributions, where the seeded population is multiplied by a factor such that the summed curve contains 6×10^3 Rydbergs from N=35 to N=200.

As the plasma expands and cools, the N_{max} cutoff clearly moves to higher and higher N-levels (simply based on the $T_e^{-1/2}$ dependence of N_{max}). As a result, the overall loss of Rydbergs due to ionization should gradually decrease, as the existing Rydberg atoms are then much lower than the N_{max} cut and new Rydberg formation rate will tend to remain constant, as the drop in density is partially offset by a drop in temperature.

3.3 Observing Rydbergs in an Ultracold Plasma

3.3.1 Field Ionization Ramps

In most systems studying Rydberg atoms, the favored technique for measuring the Rydbergs is the application of a field ionization ramp (FIR). The idea is quite simple - since Rydberg atoms have a well-understood spectrum of binding energies that simply obeys a $E_r = 13.6eV/N^2$ expression, ramping up a DC field and measuring the released electrons results in a measurement of the Rydberg population distribution as a function of the principal quantum number N. As the field strength exceeds the binding energy of a particular Rydberg level, atoms occupying that level will ionize. Thus by applying a sufficiently high electric field, the entire Rydberg population down to some field-dependent minimum N level can be ionized. By then observing the charged particles leaving the system, the Rydberg population can be measured; furthermore, since different levels ionize at different applied field amplitudes, knowing the time-dependence of the electric field ramp together with

the time-dependent charged particle signal immediately results in a measurement of the Rydberg spectrum for a given system.

Early studies of Rydberg populations in UCPs used this technique [47]. Indeed, those measurements gave an early, albeit rough, estimate of three-body recombination rates and spurred on theoretical work regarding low-temperature 3BR. However, FIRs are not ideal for UCP systems. First, they are destructive to the plasma, as a small plasma such as these will be dramatically altered due to the application of an external field, as shown by the sharp increase in electron emission from the plasma in response to even small fields. This effect also causes deterioration in the Rydberg FIR signal, as the electrons detected can be from the damaged plasma or from Rydbergs. This can potentially be remedied by first applying a modest field, such that plasma electrons are stripped but Rydbergs are unaffected, and following that with the true ionization ramp; however, this limits the highest detectable N level.

The second problem is that there is the added issue of electrons being bound to the plasma with energies similar to the binding energies of the Rydbergs in the plasma. That is, one could try to dump the plasma electrons before performing a FIR, but this is problematic at best. Because of the similarities in the two binding energies, it is not possible to remove the plasma electrons from the system without applying a field large enough to ionize some Rydbergs. Likewise, Rydbergs cannot be ionized without prompting a substantial release of electrons from the plasma system.

As an example, plotted in Fig. 3.5(a) is the self-consistent solution for the potential well of an electron in the plasma. Also shown, in Fig. 3.5(b), are the binding energies of selected Rydberg levels. It is clearly not reasonable to be able to field ionize Rydbergs in the plasma without tipping the potential such that a significant number of plasma electrons are dumped from the system along with the electrons from the ionized Rydbergs. Note that as electrons are spilled in such a manner, the potential as plotted in Fig. 3.5(a) will then deepen (as the charge imbalance will increase), thus making it possibly easier to access Rydbergs embedded in the plasma. This results in a signal that is difficult to interpret, however, as in the process the plasma dynamics are altered, affecting the Rydberg population being measured.

3.3.2 Microwave Ionization Pulses

Fortunately, there exists another technique for measuring Rydberg atoms. By applying an external microwave field, Rydbergs are driven through Landau crossings in a multi-photon ionization process [52]. On the surface, this appears to be little better than a FIR - however, microwaves are substantially higher frequency than the characteristic plasma frequencies (in our system, 2.4 GHz as compared to tens to a few hundreds of MHz). Thus, the plasma effectively does not see the microwave field, as the field is oscillating faster than the electron system can respond; that is,the electrons will vibrate at the microwave frequency, which can result in heating

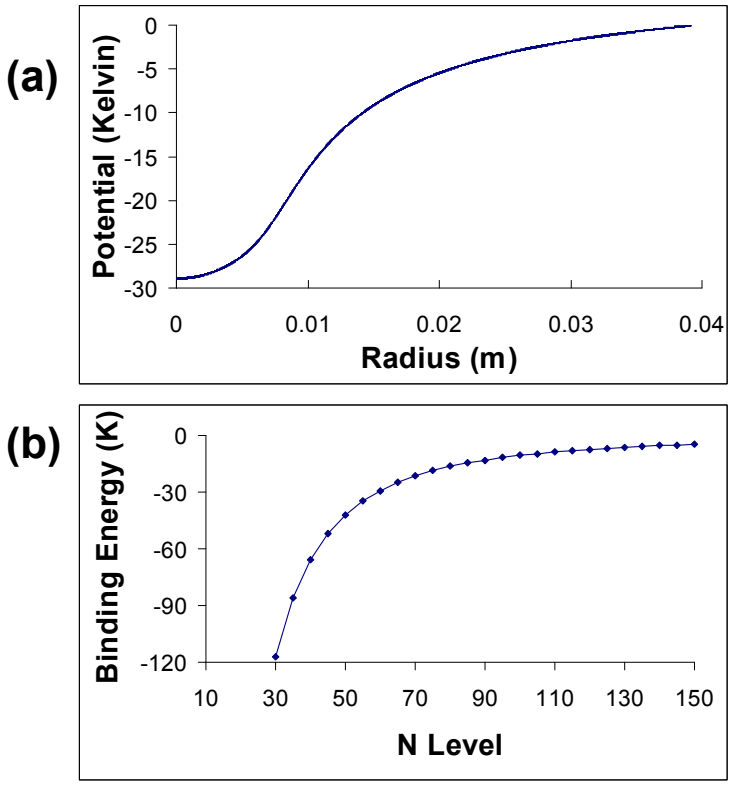

Figure 3.5: (a) The self-consistent solution for the potential (in Kelvin) seen by an electron in the plasma. Parameters used are an initial peak density of 2×10^{15} m^{-3}, initial radius of σ=280 μm, asymptotic expansion velocity v=65 m/s, time after ionization of 50 μs, electron temperature of T_e=2 K, and 76% neutrality. (b) The binding energies (in Kelvin) for Rydberg atoms at selected principal quantum numbers N.

through collisions, but our UCP system is typically of a low enough density that this may be neglected for sufficiently short applications of microwaves.

We tested this by creating a plasma with high initial electron temperature, such that Rydberg formation was strongly suppressed. Comparing the electron emission of the expanding plasma without applied microwaves to the emission of the expanding plasma while applying microwaves continuously throughout the expansion, it is clear that the two electron emission signals are similar. The electron emission signal, however, would be substantially different if the microwaves were acting as an additional heat source for the plasma. Thus, in the absence of Rydberg atoms, the plasma is effectively transparent to the microwave field. Examples of this at 3 K and 300 K are in Fig. 3.6; these curves are simply a background (no microwave field) curve at that initial electron temperature subtracted from the curve resulting when microwaves are applied for the duration of the UCP expansion. It should be noted, however, that the microwaves can have a larger heating effect on plasmas with lower initial ionization energy, as a fixed input of energy from the microwaves will have a larger relative effect on the temperature. However, this can not be tested directly, as such low energy plasmas create large Rydberg populations that are ionized by the microwaves, so that it is unclear if the observed small heating effect is due to the microwave effect on plasma electrons or to the newly ionized electrons undergoing collisions with plasma electrons as they leave the system.

The microwave ionization process is largely independent of the microwave frequency, although there are some multiphoton resonances in the Rydberg energy level structure [52]. Instead, the ionization process depends on the amplitude of the mi-

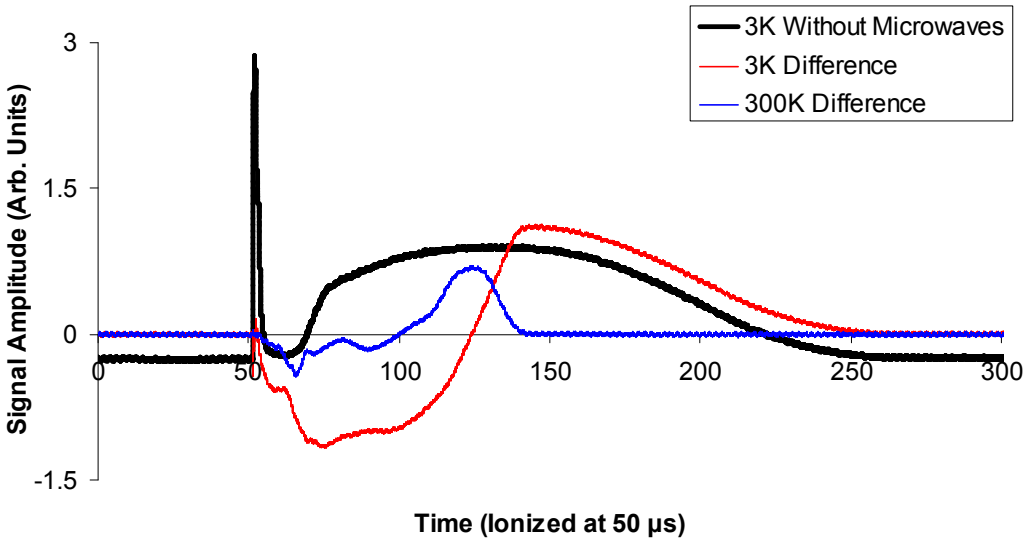

Figure 3.6: At each temperature, we obtain a curve with the microwaves constantly applied and subtract a background curve (without microwaves). The deviation at 300 K is relatively minor; however, at 3 K the deviations are quite substantial. It is not obvious whether this is because the low temperature plasmas are more susceptible to direct heating by microwaves or if it results from indirect heating by microwave ionization of Rydbergs in the plasma. However, in practice we apply very short microwave pulses to minimize any such effects. The y-axis scaling is in arbitrary units with a typical 3K curve plotted for comparison.

crowave field. It should be noted that in our system, we couple microwaves onto the top grid of Fig. 1.7; we use a vacuum feedthrough that is not impedance matched. In this microwave line, we benefit from an electronic resonance with a Q of about 400 at 2.4 GHz; we thus use 2.4 GHz microwaves to exploit this resonance and generate much larger fields than we would otherwise be capable of. A short, several-hundred nanosecond long pulse with our current equipment (microwave source, amplifier, directional couplers, and vacuum feedthrough) tuned to 2.4 GHz is capable of ionizing all Rydbergs above N=34, which is similar to the depth that our FIR can easily probe.

Furthermore, this technique can be used to obtain Rydberg population distribution information, as the FIR can, although the microwave ionization technique requires several shots to build up the population information that a FIR can obtain from a single ramp. By varying the strength of the microwave pulse, we vary the minimum N-level the pulse is able to ionize. This results in a collection of data from which we can extract the Rydberg N-level distribution; this is addressed in greater detail in Section 4.5.

This is clearly a technique preferable to FIR. It has all the strengths of a FIR (including ease of use, depth of binding energies it can probe, and the ability to extract population distributions) while additionally being non-destructive to the plasma. Indeed, the greatest effect it has on the plasma itself is indirect - by ionizing the Rydbergs, the microwave pulse appears to have a slight heating effect on the plasma electrons at times early in the plasma expansion, as the electrons leaving the Rydbergs are typically warmer than plasma electrons and undergo 1-4 collisions

while leaving the plasma [40] (based on an approximate mean free path calculation for warm electrons in the plasma). This is very minor, however, particularly compared to the highly destructive nature of a FIR.

We have successfully applied microwave ionization techniques in a UCP to extract total Rydberg populations as a function of time. We create the UCP, then apply a 1 μs long pulse of 2.4 GHz microwaves at the full power our equipment is capable of (about 14 dBm at the vacuum feedthrough). We apply this pulse at varying times in the plasma, and record the electron emission signal, averaging it over 30-60 runs. At times corresponding to the applied microwave pulse, we observe a peak in the electron emission signal due to electrons, ionized by the microwave pulse, exiting the plasma. On either side of the peak, a 1-2 μs length of the emission curve is used to fit a background line (a polynomial of order 1, 2, or 3, depending on the location of the peak on the emission curve). The area between the background line and the Rydberg electron peak is integrated (see Fig. 3.7). The total area under the full 200 μs long emission curve is also integrated, as that integration is proportional to the total number of electrons in the plasma. The ratio of these two integrals, times the total number of electrons estimated in the plasma (calculated using Eq. 1.2 with estimates for σ, n, and v, and often also multplying by the neutrality of the plasma at the time under consideration to account for the evaporative loss of electrons) results in an estimate of the number of Rydbergs ionized by the microwave pulse. The results are plotted in Fig. 3.8. One difficult region for these measurements is at late times in the plasma; often the peaks resulting from ionization overshoot when they merge back to the emission signal, effectively dipping below the emission

curve, making a background fit difficult to perform. A typical solution for this is to perform the background curve over both the up- and down-ward peaks, then only integrate the area under the ionization peak for the region where the ionization peak is actually above the background fit. Examples of these fitting techniques are given in Fig. 3.7.

As in earlier work with FIR in UCPs [47], we note odd features in these population measurements, which to date have not been well explained by theoretical work - for example, the total number of Rydbergs appears to drop in the middle of the plasma lifetime, then regrow later in the expansion (Fig. 3.8). Possible explanations, such as the bulk of the Rydbergs shifting to N-levels lower than N=34 (the lowest N we can ionize with this microwave system) [9], are not reasonable so late in the plasma expansion; plasma parameters at those times, together with the expected rate equations for the Rydberg N-levels to drop, simply do not appear to suggest the types of time-dependent Rydberg populations observed. That is, a dip in the measurable populations has been predicted in simulations [9], but at much earlier times in the plasma expansion than we observe.

The results of Figure 3.8 are important as a verification of this microwave ionization technique as a means to measure the Rydberg population in an ultracold plasma. However, further use of such measurements is limited, as it is difficult to determine the significance of total Rydberg populations due to the complicated interplay of the Rydberg processes addressed in this chapter and with the Rydbergs having radiative decay lifetimes comparable to the lifetime of the plasma itself. That is, the measurements of Figure 3.8 are effectively the time-integrated effects

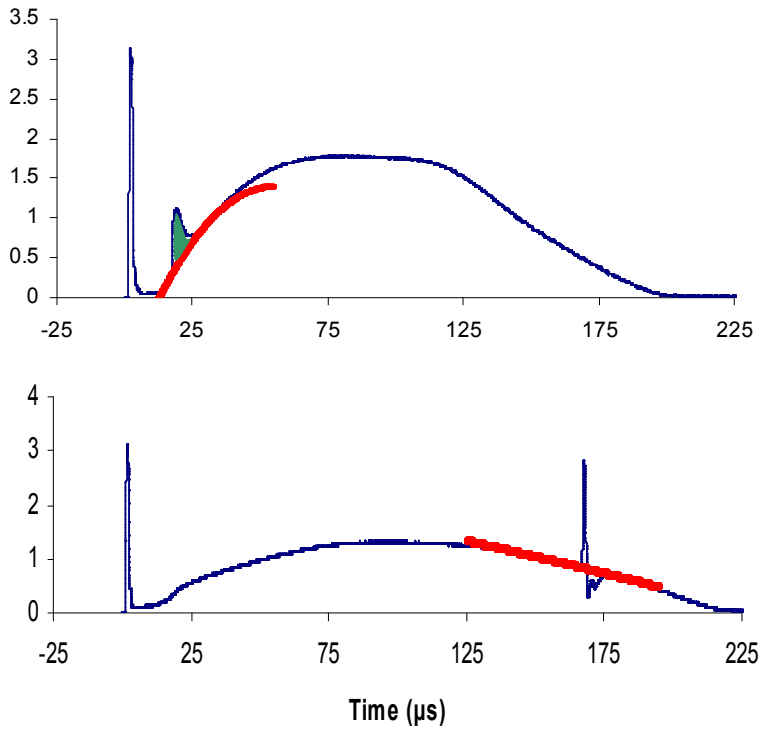

Figure 3.7: Microwave pulses applied at $t = 15\mu$s (top plot) and $t = 165\mu$s (bottom plot); the y-axis is in arbitrary units, but is proportional to the number of electrons striking the MCP in each time interval. For each curve, the electron peak caused by the ionization of the Rydbergs is obvious. A background fit is done for each (dashed red lines) and the region between the Rydberg peak and the background is integrated (seen in top plot; peak in bottom plot is too narrow for illustrating this). The late-time pulse in the bottom plot indicates a difficulty with detecting Rydbergs at late times; the pulse drops below the background curve. That region is neglected when taking the integral of the Rydberg peak. Also observable is the heating effect that the ionized Rydbergs have on the early plasma, as the plasma lifetime in the upper plot is shorter than the lifetime in the lower

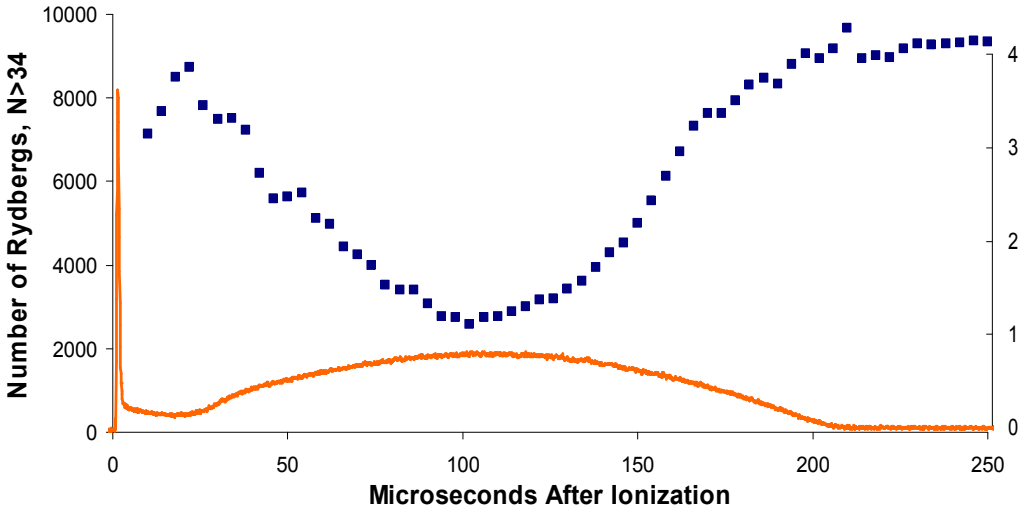

Figure 3.8: Measurements of Rydberg populations in an UCP as a function of time, using a single microwave pulse (duration of 1 μs) stepped through the plasma lifetime. Note that the y-axis is scaled as Rydberg counts for the population measurement (blue squares), while the solid curve has arbitrary y-scaling (right vertical axis) and is simply plotted to provide a reference to the expansion of the plasma. The error associated with these population measurements is approximately 5%.

of all such Rydberg processes together with the strongly-changing plasma dynamics (particularly as they affect densities and temperatures), requiring a very complicated model to extract useful information from such measurements.

Chapter 4

Three-Body Recombination Measurements in Ultracold Plasmas

4.1 Overview

As discussed in Section 3.3.2, the microwave ionization technique has been demonstrated as a viable means to measure the number of Rydbergs in an ultracold plasma in a manner that does not destroy the plasma itself. Measurements such as Figure 3.8 are difficult to use, however, as such time-dependent population measurements are the result of plasma evolution together with the many Rydberg processes discussed in Chapter 3.

However, because microwave ionization techniques do not destroy the plasma, a pair of microwave pulses can be used for more effective measurements. The first pulse essentially clears out the Rydberg population for N>34 (as determined by the maximum microwave field we can apply), while the second pulse then probes how many Rydbergs are present after some time delay δt. This clearly provides a means to measure the Rydberg formation and thus the three-body recombination rate in ultracold plasmas.

Another change to the microwave ionization technique that is of potential use is to vary the microwave power in the pulse. This changes the minimum N-level that can be ionized by the pulse. This then allows the measurement of the Rydberg population distribution as a function of N. By combining this concept with a double-

pulse experiment, the distribution of Rydbergs created by three-body recombination can be directly determined.

4.2 Three-Body Recombination Rates: Background and Proposed Corrections

Mansbach and Keck developed the widely accepted rate expression for three-body recombination (Eq. 3.1) [1] and other groups have developed similar rates (for example, [51]). They used detailed balance together with Monte Carlo simulations to develop rate equations for both electron-Rydberg collisions and three-body recombination. It should be first noted that the rate coefficient K has roughly 10% uncertainty (as determined by [1]). Other derivations of this rate have similar uncertainties due to the use of the approximated Coulomb logarithm [53]. The Mansbach and Keck rate has been experimentally verified at higher temperatures [54, 55]; however, recent theoretical work has addressed the validity of the rate expression at low temperatures.

As previously discussed, because of the finite depth potential seen by the electrons, the electron distribution can not be strictly Maxwell-Boltzmann; replacing the Maxwell-Boltzmann distribution for the electron velocities with a Michie-King distribution (often used in astrophysics for distributions like the velocities of stars in globular clusters, it is essentially a Maxwell-Boltzmann distribution shifted by a fixed energy such that it is zero for a finite energy and is zero for all energies greater than that; this is simply a means to truncate the Maxwell-Boltzmann distribution

to eliminate the infinite-velocity tail) results in a multiplicative correction factor to Eq. 3.1 of only 1 to 1.1 [46]. This particular correction is therefore very minor for our particular system and likely can be disregarded, particularly as it is smaller than the spread in typical estimates for the rate coefficient K. An example of this is given in Fig. 4.1.

Another potential correction is to modify the high-N cutoff used in [1]. Eq. 3.1 was developed by assuming that there was a maximum allowed N-level that could form through three-body recombination; this level was linked to the electron temperature and gives rise to the strong T_e dependence in the expression. The cutoff could be altered to be dependent on the plasma density [42]; however, this particular correction is only applicable to systems with higher densities (by several orders of magnitude) than our xenon plasma. That is, this is a correction for strongly coupled plasma systems, while our electron system is weakly coupled, as indicated by theoretical work [11] as well as electron temperatures measurements [32].

Some work has been done indicating that, at temperatures below $\sim$ 1000 K, quantum 3BR effects should populate N levels lower than those populated by the classical 3BR rate expression, Eq. 3.1. These calculations [56] did not go below $T_e \sim 100$K, so direct comparison with measurements in our system is currently not possible.

Work in progress by some theorists addresses some of the fundamental assumptions made by [1] that limited the parameter range over which Eq. 3.1 is valid. Essentially, more comprehensive Monte Carlo simulations were run over a wider range of energies than those investigated in [1]. This also involves a differing

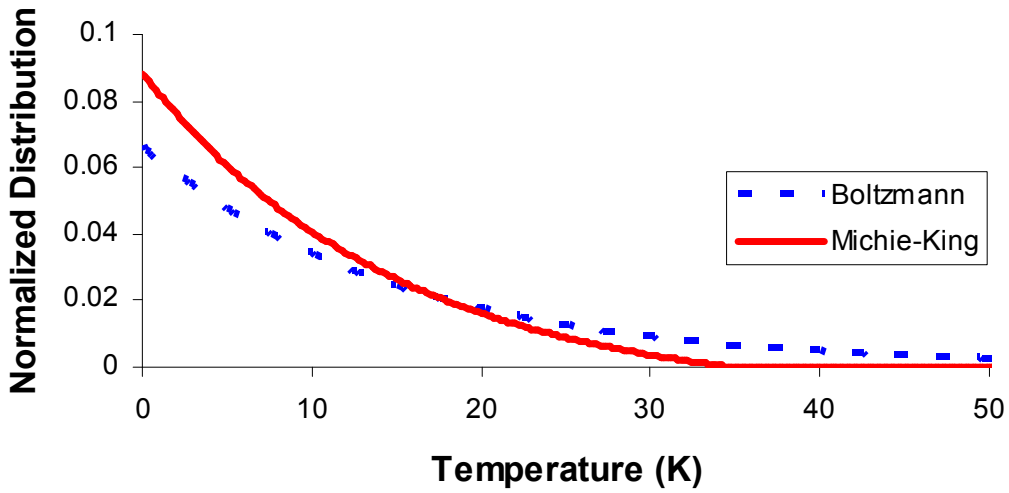

Figure 4.1: Comparison of the Maxwell-Boltzmann (MB) energy distribution with the Michie-King (MK) distribution. Both distributions are at $T_e = 15$ K. The MK is simply the MB distribution offset by the potential energy at infinity (in this case, I picked 35 K, purely for illustrative purposes, as typically the differences in the distribution will be much smaller than shown) and set to zero for energies greater than this offset. The integrals of both distributions are normalized to unity.

treatment of the high-N cutoff N_{max} that was formerly an *ad hoc* addition to 3BR theory; instead, the cutoff is treated using explicit ionization arguments rather than an assumption of ionization. A cutoff similar to the commonly used N_{max} was obtained using this more thorough approach. The resulting rate expression [57] results in Rydberg atoms forming with a population having a different N-dependence (N^4 instead of N^6) as well as a somewhat different rate expression overall. See Figure 4.2.

4.3 Measuring Three-Body Recombination Rates in Ultracold Plasmas

While microwave pulses are a very effective way of detecting and counting the number of Rydberg atoms embedded in ultracold plasmas, a single pulse does not effectively convey information regarding a single rate in the plasma, due to the complex nature of Rydberg atom dynamics in UCPs. Instead, we use a double pulse to measure three-body recombination. The first pulse (approximately 200 ns in duration) clears the plasma of all Rydberg atoms with N>34. A second pulse, identical to the first, is then applied after a variable delay δt. Because all Rydbergs with N>34 were previously ionized and because, at all times after ionization that we consider, upward shifting processes for N<34 are suppressed due to $34<N_{=}$ throughout the plasma lifetime (Figure 3.2), all Rydbergs ionized by the second microwave pulse should be due to Rydberg-creating processes, provided δt is short. Since the only such process of any significance in a UCP is three-body recombination,

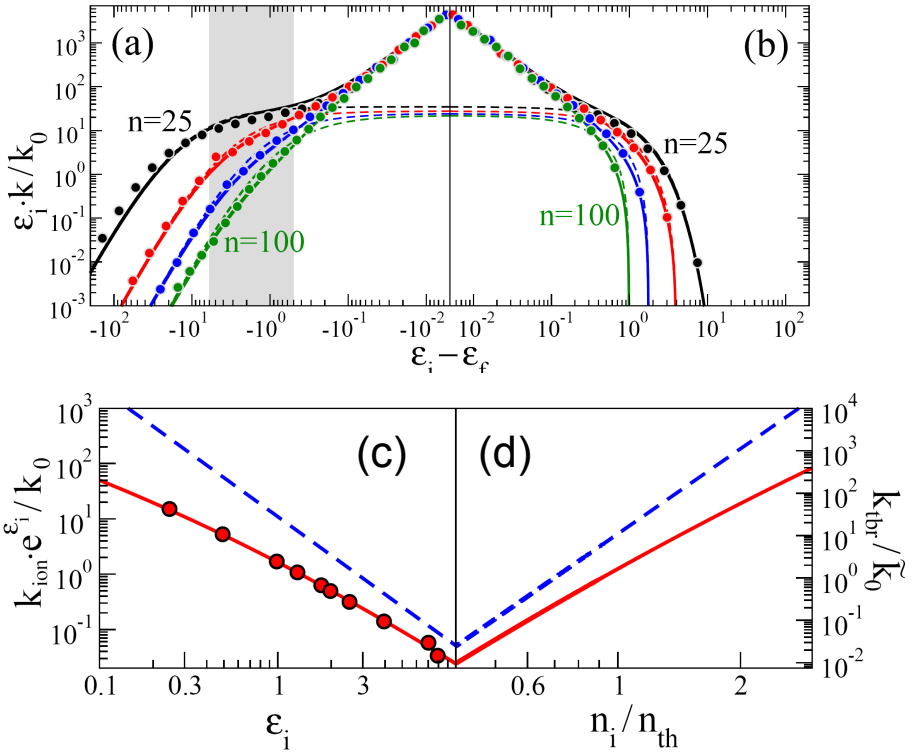

Figure 4.2: Comparison of Mansbach & Keck rates with those calculated by Pohl, used with permission from [57]. Rate coefficients for de-excitation (a) and excitation (b) due to electron-Rydberg collisions at $T_e = 16$ K. ϵ_i and ϵ_f are the initial and final state energies, respectively, where $\epsilon = 13.6\text{eV}/n^2_{i(f)} k_b T_e$. (c) and (d) are the ionization and 3BR rates, respectively. Symbols are Monte Carlo results by Pohl, solid lines are fits to those results, and dashed lines are the results of [1], with the region investigated by [1] shaded in part (a).

the population measured by the second pulse divided by the delay δt is therefore a measurement of the three-body recombination rate.

This technique is somewhat challenging, given the short delays between the two pulses that are required; for long delays of a μs or longer, the N>34 population begins to be strongly affected by level-shifting processes, such that the populations measured are no longer simply due to 3BR but may be altered due to a loss of the created Rydbergs to either ionization or down-shifting of N-levels. Because of this challenge, together with the typical signal-to-noise difficulties associated with shot-to-shot noise in the system, we actually use a collection of measurements using different delays (δt) (see Figure 4.3) and perform a linear best-fit to the collection. The slope is then the three-body recombination rate. The linear best-fit is typically limited to delay times of less than 750 ns, as for delay times greater than this the refill curve is no longer linear due to non-3BR effects beginning to turn on.

To measure the populations we apply the double pulses to the plasma with varying delays between the pulses. Each delay measurement is repeated 30-60 times and the plasma signals are averaged to improve signal-to-noise. The emission peaks due to the microwave pulses are identified; however, because of the short delays involved, the two peaks are close enough together to broaden into one another, resulting in a single peak. Short times on either side of the peak (1-2 μs) are then used to fit a background curve (usually using a polynomial of order 1, 2 or 3, depending on where in the plasma expansion the measurement is performed), approximating the shape the electron emission curve without microwaves (a simple background subtraction is often not feasible, due to drift in the experiment or because of the minor

heating effects of microwaves on the plasma at early times in the plasma expansion causing a no-microwave field curve to be different from the curves resulting with applied microwaves). The area under the microwave-induced peak and above the background curve is then integrated. We calculate the number of electrons detected in this peak (and thus the number of ionized Rydbergs) by multiplying the total number of electrons expected in the plasma by the ratio of the area just obtained to the total area under the full electron emission curve. This is effectively the same technique for counting Rydbergs in the signal as was described in Section 3.3.2 and illustrated in Fig. 3.6. Keeping in mind that this peak is really due to the contributions from both the clear and probe pulses, this is repeated for several delays and, under the assumption the clear pulse contribution remains roughly constant, the change in the signal is therefore the result of the change in the probe pulse contribution. We are interested in the slope of the best-fit line, which will correspond to the 3BR rate. There is an offset on this data which will be proportional to the total number of Rydbergs in the plasma at the time of the measurement (the time-dependent offset is similar to the measurement of Fig. 3.8).

After performing this several times over a range of times after ionization, we obtained a collection of widely varying three-body recombination rate measurements (Fig. 4.4). To improve the statistics, we binned the rate measurements with respect to time and averaged in both time and rate measurement. The resulting 3BR rate vs. time plot (Fig. 4.5) still has significant uncertainties, but several features still stand out. First, all of the measured rates of Fig. 4.5 are within a factor of three of one another. Second, the rate appears to shift from an early, higher 3BR rate

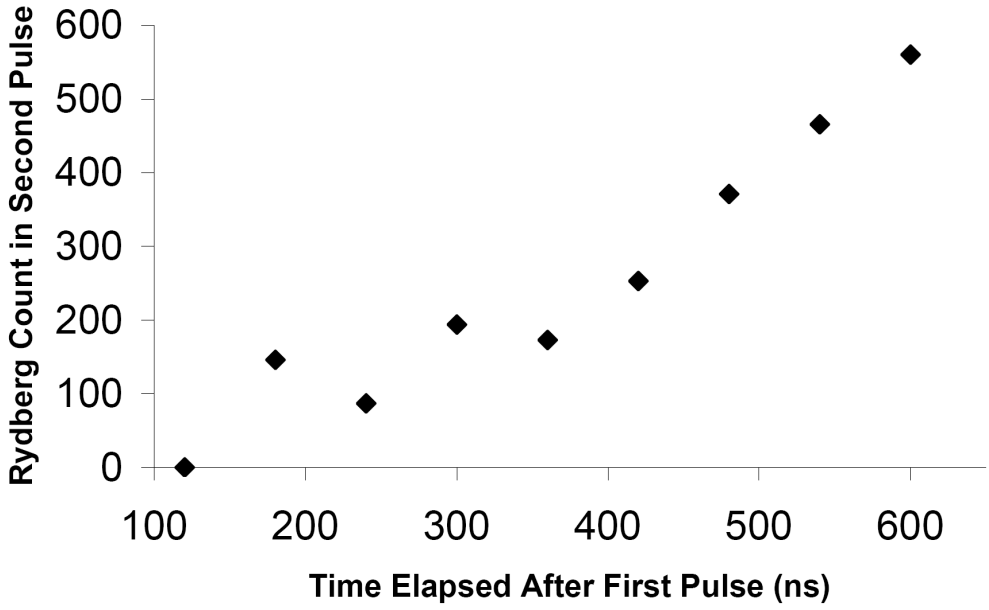

Figure 4.3: An example of the Rydberg refill curve, taken 55 μs after ionization. A linear best fit to these points will have a slope equal to the three-body recombination rate. This data was taken by applying a clear pulse of microwaves, ionizing all Rydbergs with N>34. After a short delay, a second pulse was applied to probe the number of new Rydbergs with N>34 in the system. The number of such Rydbergs is plotted above as a function of the delay time, with the offset due to the clear pulse subtracted out. Uncertainties for each point are approximately 30%, so typically we fit straight lines to several such plots and average the fitted slopes.

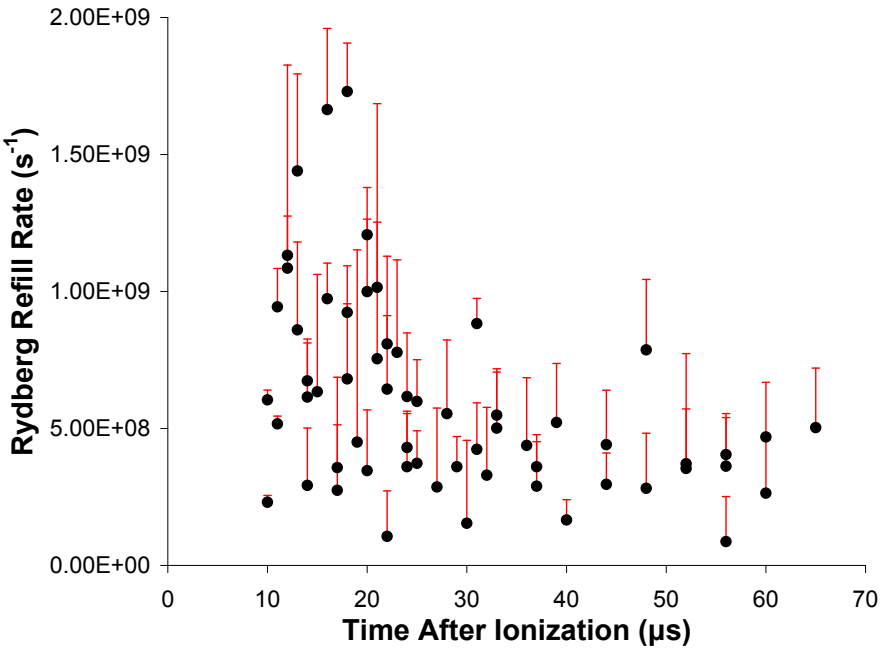

Figure 4.4: Measurements of the Rydberg refill rates at different times in the plasma expansion. Errors are only plotted in one direction; similar downward errors in the rates are present, but are not plotted. To the best of our knowledge, these are the first measurements of three-body recombination rates at temperatures below 300 K.

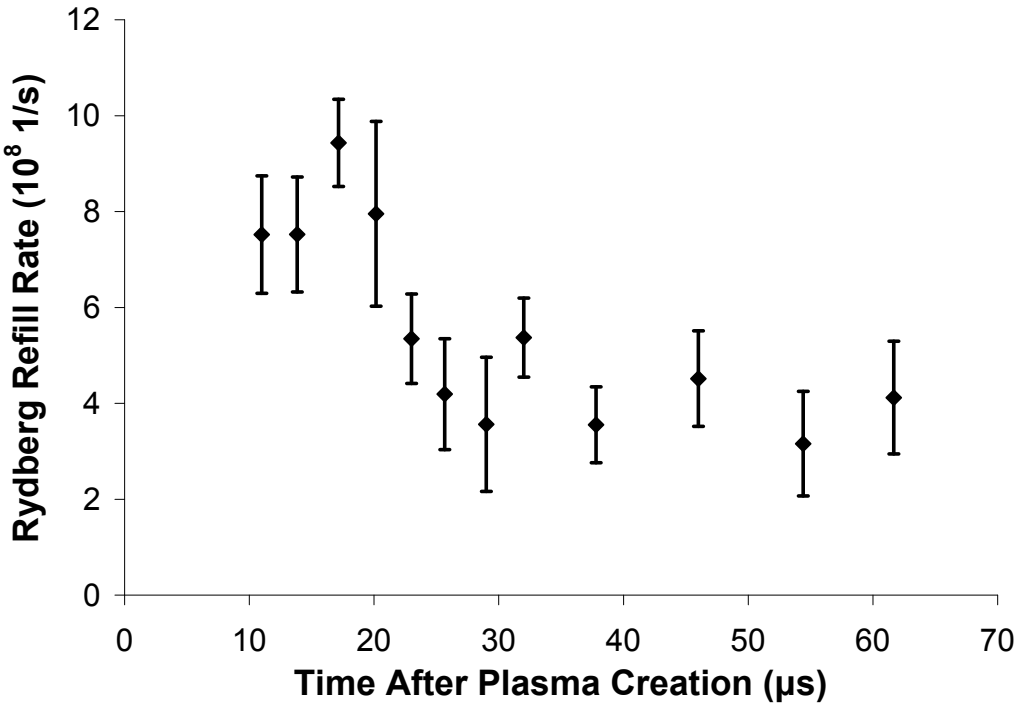

Figure 4.5: The time-binned and averaged Rydberg refill rates, based on the measurements in Figure 4.4.

to a lower rate at about 40 μs. Third, after that shift, the rate appears constant or slightly declining. The first feature is of great interest, as the plasma densities have dropped by two orders of magnitude between 10 μs and 50 μs while 3BR scales as n_e^2. The second feature is still unexplained and is thus of interest. The third feature is possibly indicative of a thermostat effect; so late in the plasma, the electron temperature changes are expected to be dominated by adiabatic expansion effects. As the electrons cool due to adiabatic expansion, 3BR turns on (due to the $T^{-9/2}$ dependence) and begins to heat the plasma, counteracting the cooling effect to some degree (and thus stabilizing the rate of 3BR).

This set of measurements represents, to our knowledge, the first measurement of three-body recombination in weakly-coupled neutral plasmas at temperatures below 10 K. Some 3BR measurements have been made at temperatures as low as $\sim$ 25 K [58] in a helium plasma discharge. We note some $\sim$ 10 K measurements have been made in beam environments with highly ionized ions and electron coolers, although these are typically in magnetic fields or are strongly-coupled and therefore should measure substantially different rates [59, 60]. Our measurement of the 3BR rate has the potential to be the strongest test case for low-temperature 3BR theories available. This potential, however, is contingent on better electron temperature measurements being available for these systems. That is, while the 3BR rate has been measured and good estimates for the electron and ion time-dependent spatial densities exist, Eq. 3.1 depends on electron temperature in a $T_e^{-9/2}$ manner; thus, without very good electron temperature measurements, it is impossible to say with

any certainty whether a given theoretical rate expression is a valid description of the measured 3BR rates.

4.4 Three-Body Recombination Rates as Electron Temperature Measurements

A feature of Eq. 3.1 that cannot be stressed enough is its strong dependence on electron temperatures. While this means very good electron temperature measurements are needed if one is to compare that equation to measured three-body recombination rates, we can invert the expression and instead attempt to use the rate measurements as a means to calculate the electron temperatures:

$$T_e(t) = \left[\frac{R_{3BR}(t)}{K_{3BR}\int n_e^2(r) n_i(r) 4\pi r^2 dr}\right]^{-2/9} \tag{4.1}$$

It is obvious that this is not a good means for determining the electron temperatures if the rate expression itself is substantially incorrect. However, most theory work indicates that major deviations from Eq. 3.1 (such as a change in the exponent on the electron temperature term) should only be the result of having a strongly-coupled electron system. As our system appears to be solidly in the weakly-coupled regime, the rate expression is likely fundamentally correct; this is supported experimentally, as 3BR rates calculated with Eq. 3.1 and using the electron temperature measurements of [32] (see Fig. 2.2) have high uncertainties, but are consistent with measured 3BR rates. Minor deviations from the rate expression (such as a change

in the rate coefficient K_{3BR}) are possible, but are strongly suppressed by the -2/9 exponent in Eq. 4.1. This approach, therefore, is actually very robust, as the -2/9 exponent suppresses experimental uncertainties in measuring R_{3BR}, any uncertainties in the rate coefficient K_{3BR}, and modest changes to the form of the rate equation itself.

By using our measured 3BR rates (Fig. 4.5) with the inverted 3BR rate equation (Eq. 4.1), we calculate the time-dependent electron temperatures, as plotted in Fig. 4.6. Our calculated temperatures are diamonds (also in the inset plot), while we include simulation results by F. Robicheaux [40] (triangles) and the temperature measurements by J. Roberts [32] (squares) for comparison.

This provides the first low-uncertainty, late-time measurement of the electron temperature in ultracold plasmas. The extracted temperatures are extremely low, even dropping below 1 K at about 50 μs (and extrapolating to the end of the plasma lifetime, this curve might suggest temperatures as low as 200 mK at the 200 μs point of the plasma expansion); these are the lowest T_e observed in an ultracold neutral plasma. It should be noted that Fig. 4.5(b) indicates electron Coulomb coupling parameters well below 1, which is consistent with theoretical predictions for our system, other measurements of the coupling parameters in UCPs, and the assumption that our system is weakly coupled (an assumption integral to the use of Eq. 4.1 for these temperature calculations). The measured temperatures have a fitted time-dependence that goes as $t^{-1.2\pm.1}$. This is substantially different than the t^{-2} expected from adiabatic cooling alone. The difference is possibly due to the heating effects of three-body recombination; cooling due to adiabatic expansion

will tend to increase the rate of 3BR, which in turn heats the plasma and turns off the increase of 3BR. Thus, at later times in the plasma, the 3BR rate should be roughly constant (as was measured), which according to Eq. 4.1 will result in a time-dependence like $t^{-4/3}$ (as the integral term in the equation has the form t^{-6}).

4.5 Rydberg Population Distributions Due to Three-Body Recombination

Recent theoretical work by Pohl [57] suggests a somewhat different form for the three-body rate expression. His proposed rate is somewhat lower than that of Mansbach and Keck and could affect our use Eq. 4.1 in calculating electron temperatures; however, as the two rates are less than a factor of 5 different for the parameters typical of our system (see Fig. 4.7), this modification would only alter our electron temperature calculations by, at most, 40%. Note the same holds true for the other 3BR rate shown in Fig. 4.7; we have not addressed the Vriens and Smeets rate expression [61], but the differences between the three pictured rate predictions is indicative of the types of uncertainties present in 3BR rate expressions.

The xenon ultracold plasma provides a good environment for testing this new rate expression proposed by Pohl. However, the lack of good electron temperature measurements (independent of any three-body recombination rate measurements) continues to make such experimental verification of theoretical rates problematic.

One approach is available for testing the rate expressions. The Mansbach and Keck expression results in three-body recombination generating Rydberg atoms with

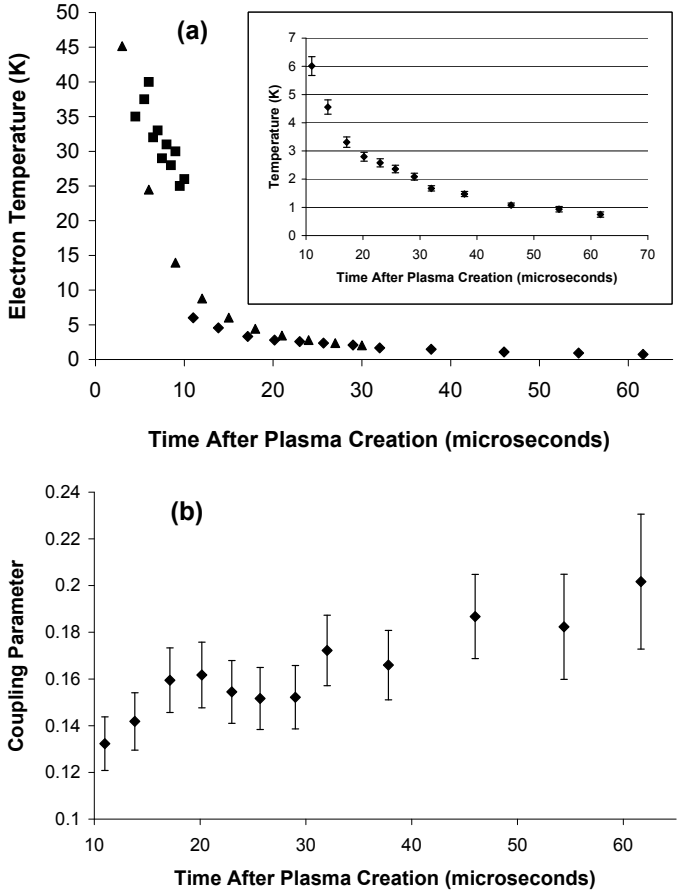

Figure 4.6: (a) The UCP electron temperatures (diamonds; also inset), computed using Eq. 4.1 together with the 3BR rate measurements of Fig. 4.5. Also plotted are the earlier temperature measurements of [32], as seen in Fig. 2.2. The triangles are the results of temperature simulations by F. Robicheaux. (b) The electron-system Coulomb coupling parameter Γ, calculated using the T_e of part (a). This shows the temperature measurements of part (a) are consistent with earlier work indicating the electron system is weakly coupled and indicating self-consistency with the assumption that Eq. 4.1 is fundamentally correct, as proposed changes to it are typically valid only for a strongly coupled system.

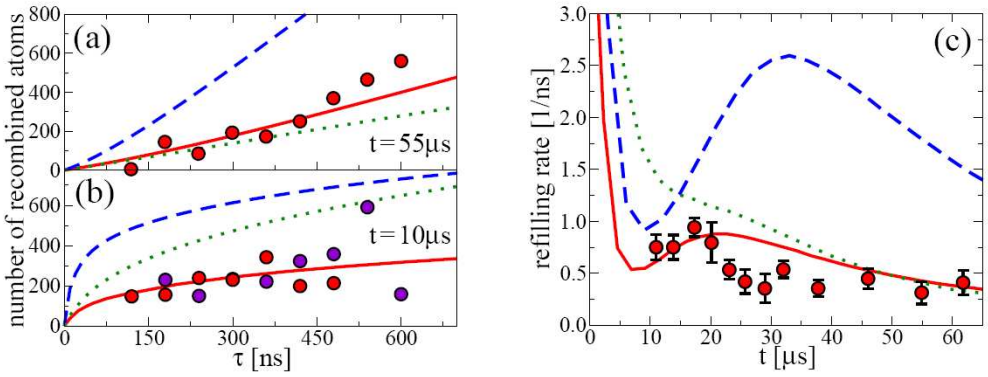

Figure 4.7: (a) & (b): 3BR refill curves at t=55 μs and t=10 μs, similar to Fig. 4.3. The circles are Rydberg population measurements we made. The solid curve is the predicted refill using the 3BR rates recently proposed by Pohl. The dashed curve is the refill predicted by using Mansbach and Keck's rate expression. The dotted curve is the refill curve predicted by a semi-empirical formula by Vriens and Smeets [43]. (c): The 3BR rates at varying times in the plasma, similar to Fig. 4.5. Again, circles are our measurements, the solid curve is the prediction by Pohl, the dashed curve is the prediction by Mansbach and Keck, and the dotted curve is the prediction by Vriens and Smeets. Used with permission from [57]

.

a population distribution varying with the principal quantum number N as N^6, with a cutoff in the distribution at $N_{max}=\sqrt{13.6\text{eV}/2k_BT_e}$. However, the Pohl expression predicts a population distribution due to 3BR that varies as N^4, with a cutoff at a similar N_{max}. It is clear that measuring the Rydberg distribution due to 3BR can be a potentially definitive means to verify one or the other expression; this is of particular use, as comparing the Rydberg distributions will eliminate the need for good (better than about 5%) electron temperature measurements in order to verify one of the expressions.

Such a measurement can be performed by modifying the double-pulse technique described in Section 4.3. Using a very fast (switching speeds < 10 ns) voltage-controlled microwave attenuator, the measurements of Section 4.3 can be repeated while varying the power in the second (probe) microwave pulse. Recalling that higher microwave power allows the ionization of Rydbergs down to a lower N-level, it is clear that by varying the probe pulse power, the Rydberg population is being probed to varying depths:

$$P_{Ryd}(N_{min}) = \int_{N=N_{min}}^{N=N_{max}} \rho_{Ryd}(N)dN \tag{4.2}$$

where $P_{Ryd}(N_{min})$ is the Rydberg count measured in the apparatus, ρ_{Ryd} is the actual N-dependent Rydberg population distribution in the plasma, and N_{min} is the lowest N-level ionizable with a given microwave power. This allows a simple numerical derivative to be used to extract the population distribution itself:

$$\rho_{Ryd} = \frac{d}{dN_{min}} P_{Ryd}(N_{min}) \tag{4.3}$$

For an example of the calibration used for this type of measurement, see Appendix B.

As a test of this technique, we applied a single microwave pulse to the plasma at varying times. Varying the power of that pulse, P_{Ryd} can be mapped out as a function of time, in turn allowing the calculation of ρ_{Ryd}. This technique (for t=15 μs) is illustrated in Figure 4.8.

Figure 4.9(a) shows Rydberg distributions at various times in the plasma. Early-time distributions (15, 75 μs) have the distinct, characteristic low-N shelf indicative of Rydberg populations strongly dominated by collisional processes and less dominated by 3BR. However, at late times (135, 165 μs) a clear higher-N bulge forms around N=70. This may be an indication of 3BR rates increasing relative to level-shifting collisional rates, as the Rydbergs that form at high N then survive longer before ionizing or shifting down in N due to collisions. This has yet to be studied in great detail, however.

These single-pulse varied-power measurements are consistent with earlier measurements of the total Rydberg number, but have the additional benefit of breaking down that total Rydberg count into a population distribution. The next step is to attempt to determine the population distribution that is created by three-body recombination.

To do this, we combine this idea of varying pulse power with the double-pulse experiments for measuring three-body recombination rates, as described earlier. The first pulse, at full microwave power, clears out all Rydbergs with N>34. The second pulse, applied a short time after the end of the first pulse and with varying microwave

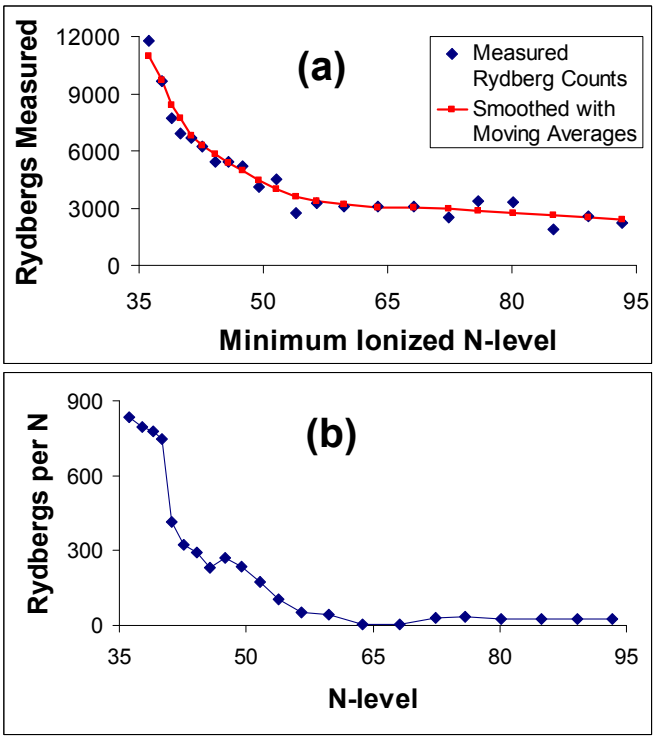

Figure 4.8: (a) Measurements of P_{Ryd} obtained by varying the microwave power, which changes the N_{min} that can be ionized. The measurements are smoothed using a 5-point moving average in order to facilitate the next step in determining the Rydberg distribution - a numerical derivative. (b) The derivative of the smoothed curve in part (a). This gives the number of Rydberg atoms per N-level as a function of N-level; that is, the Rydberg population distribution. This measurement was made 15 μs after ionization.

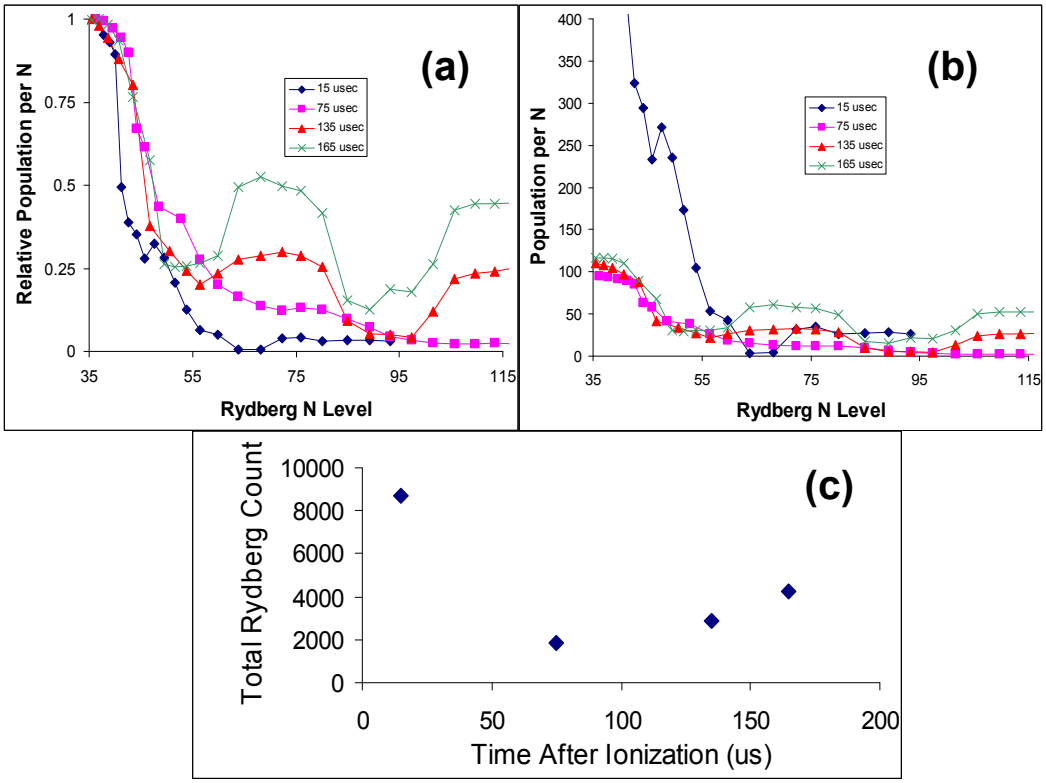

Figure 4.9: (a) The Rydberg population distributions at varying times after ionization, normalized such that the population in the N=35 state is 1 in order to easily compare the relative distributions at different times to one another. (b) The non-normalized population distributions. The t=15 μs curve is off-scale at low N, but is fully represented in Figure 4.8. (c) The integrals of the curves in part (b). This is to verify the total Rydberg populations are at least roughly consistent with other measurements such as Figure 3.8.

power, then samples the Rydberg population system in the manner illustrated in Fig. 4.8. Since this Rydberg population sampled by the probe pulse should be predominantly due to 3BR, this technique is therefore a direct probe of the Rydberg distribution that results from 3BR. This work is still in progress; a preliminary result is given in Fig. 4.10.

The results in Fig. 4.10 are intriguing. They were made early in the plasma (15 μs after ionization). Note that the shortest delay (200 ns) has a fundamentally different Rydberg population distribution (which is a repeatable feature and not due to a poor data set) than measurements with a longer delay between pulses; this short delay measurement also has some qualitative similarity to the late-time single pulse measurement of Fig. 4.9(a). Because this was done very early in the plasma lifetime, the Rydberg level-shifting processes have relatively high rates compared to three-body recombination. We likely are sampling Rydberg populations that have been altered by such level-shifting processes, such that these distributions are not due to 3BR alone. The 200 ns curve appears to be the closest to the type of 3BR distribution expected; however, given that the 400 ns curve is already indicative of electron-Rydberg collisions, a true 3BR distribution measurement would likely have to be done with a delay even shorter than 200 ns. With current equipment, that becomes a challenging technical problem.

Note that, taking the first five points in the 200 ns delay curve and fitting a power law to it, the lower-N portion of the curve has a $N^{4.9\pm0.15}$ dependence. This is in between the distribution due to [1] (N^6) and that proposed by Pohl (N^4). Thus, even this preliminary result shows some promise as a means to help resolve some of

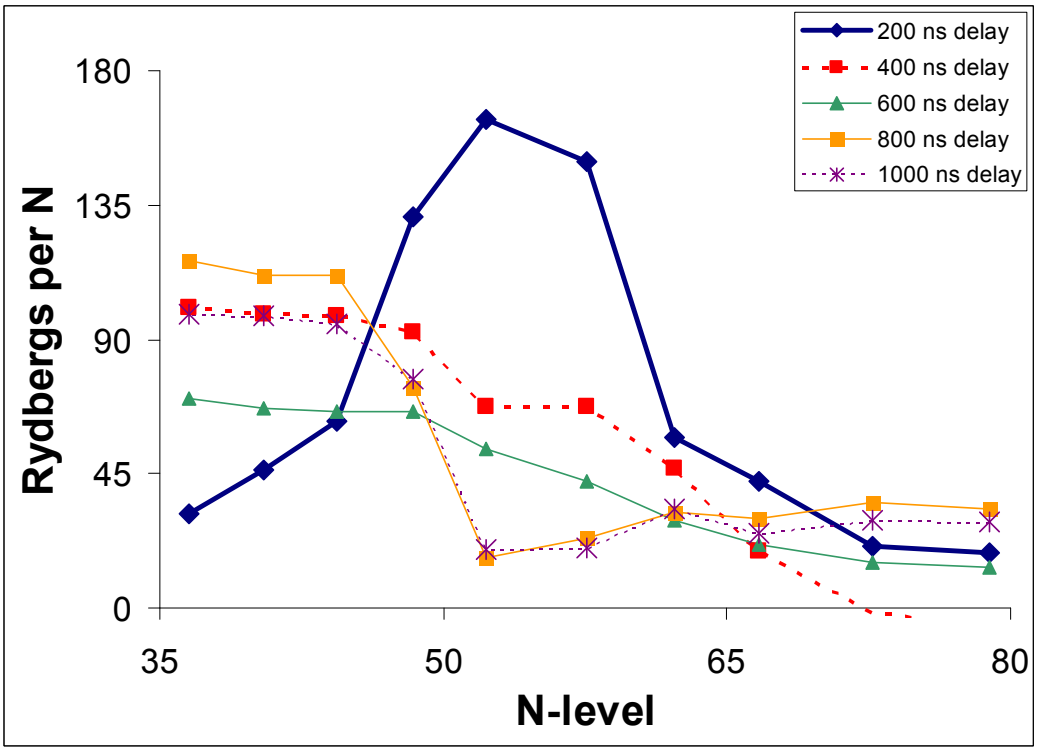

Figure 4.10: The Rydberg population distribution due to refilling at 15 μs after ionization. The delay is the amount of time elapsed between the clear pulse (at full power) and the probe pulse (with varied power). From run 121307.

the debate regarding three-body recombination rates, although clearly more work needs to be done.

Since the general N-dependence of the Rydberg population distribution due to 3BR should not be strongly dependent on when in the plasma expansion it is measured, the next step in this work (currently underway) is to repeat the measurements in Figure 4.10 at late times in the plasma. This will serve to suppress the level-shifting processes, as both temperature and density will be reduced. Three-body recombination will still occur, however, so late times in the plasma expansion (perhaps t=150 μs) are likely ideal for this measurement, as level-shifting rates will be suppressed more than 3BR.

4.6 Summary

A central outstanding problem in ultracold plasma physics is measuring the electron temperatures with low uncertainty. Existing T_e measurement techniques, in addition to having large uncertainties, have the additional problems of relying heavily on simulation results or only being applicable for a short time during the plasma expansion. Our method of measuring T_e by exciting Tonks-Dattner resonances and fitting the predicted Tonks-Dattner resonances to those resonances we observe in the plasma has the benefit of being valid much later in the plasma expansion time than other available techniques. It still has the drawback of having a high degree of uncertainty in the measurement; however, with proper treatment of the outer turn point for these electron waves, this technique may move beyond a proof-of-principle

measurement and begin to provide high-quality estimates of T_e.

In an attempt to assess the validity of low-temperature three-body recombination rate predictions, we present the lowest temperature measurements of three-body recombination in weakly-coupled neutral plasmas. The strong inverse dependence this process has on the electron temperature prevents us from using these measurements to make a definitive conclusion regarding the validity of the three-body recombination rate expressions; however, inversion of the rate expressions provides an alternate means to estimate electron temperatures. In this case, the strong inverse temperature dependence of the three-body rate expression serves to suppress experimental uncertainties as well as modest inaccuracies of the rate expression itself, such that the resulting electron temperatures have very low uncertainties.

Future work based on these results will focus on alternate means of testing the three-body recombination rate expression. By measuring the population distribution of Rydbergs formed by three-body recombination, we can test the rate expression itself without requiring accurate knowledge of the electron temperatures. Such verification will further support the use of three-body recombination rate measurements as a means of measuring the electron temperatures. Alternately, theoretical support for the Tonks-Dattner resonance technique of measuring electron temperatures could result in electron temperature measurements with sufficiently small uncertainties to directly test the validity of the three-body recombination rate expressions at low temperatures.

Appendix A

MCP Spatial Resolution as a Measurement Technique

While xenon UCPs suffer from an inability to optically image the ion distributions, there still exists a means to obtain spatial information about the plasma. Using a multi-channel plate (MCP) charged-particle detector with a phosphor screen and a frame-grabber, pictures may be taken of the spatial distribution of the charged particles striking the MCP. This is potentially more useful than the absorption or fluorescence imaging used in UCPs of other elements, as the MCP technique can be applied to either electrons or ions, and can be used at later times in the plasma expansion when the densities are too low for effective use of the two optical techniques.

This will address imaging the ions using the MCP. The electrons are, in principle, imaged in an identical manner (with obviously different voltages used). This technique has been primarily used by Xianli Zhang in our xenon system and is included here as further justification for the approximation of Eq. 1.2.

At varying times in the plasma expansion, a high-speed, high-voltage pulse ($\sim$ 400 V with a 6 ns turn on time) is applied to the grid above the UCP. This has the effect of accelerating the ions toward the MCP and removing the electrons from the system. The ions strike the MCP with some spatial distribution; this lights up the phosphor with the same distribution in intensity and a picture is taken. The

resulting image is then fitted using a 2-D Gaussian, and the resulting size as a function of time is determined. Some examples are shown in Figure A.1.

This technique clearly can image the ions at very late times. Any data obtained must be multiplied by a scalar that is dependent on the voltages on each grid; this is simply a magnification factor due to charge lensing. There exists one problem at short times - because the ions are pushed to the MCP while the electrons are stripped from the system in the opposite direction, the ions undergo a Coulomb explosion effect while in transit to the MCP. Their time of flight is typically 8 μs, resulting in an expansion much greater than simple ballistic expansion will account for. This can easily be seen at early times in Fig. A.2. We can compensate for this effect with a simple model of the Coulomb-driven acceleration term, so that the corrected sizes closely match the solid line of Fig. A.2.

It is clear that this technique matches the results obtained by other means [16, 17] yet can be applied to much later times in the plasma expansion. The sizes deviate at later times from the simple ballistic expansion model, most likely due to the physical size of the plasma getting large enough to be influenced by the non-uniform fields near the walls of our vacuum chamber.

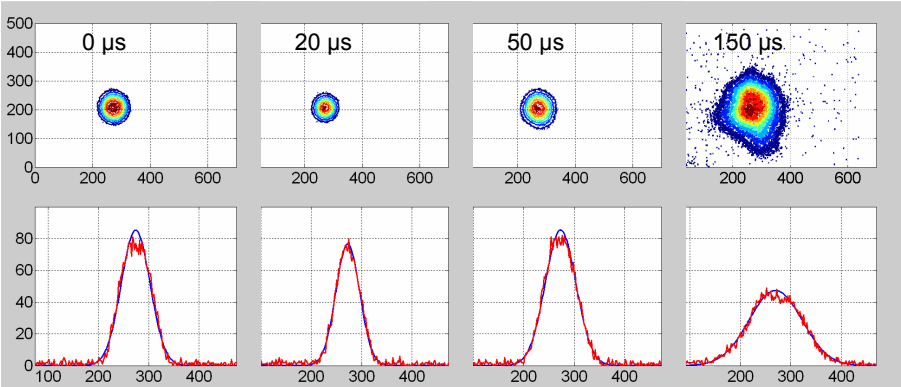

Figure A.1: MCP images of the ion distribution in the plasma as a function of time. Axis are in pixels; each pixel is about 120 μm.

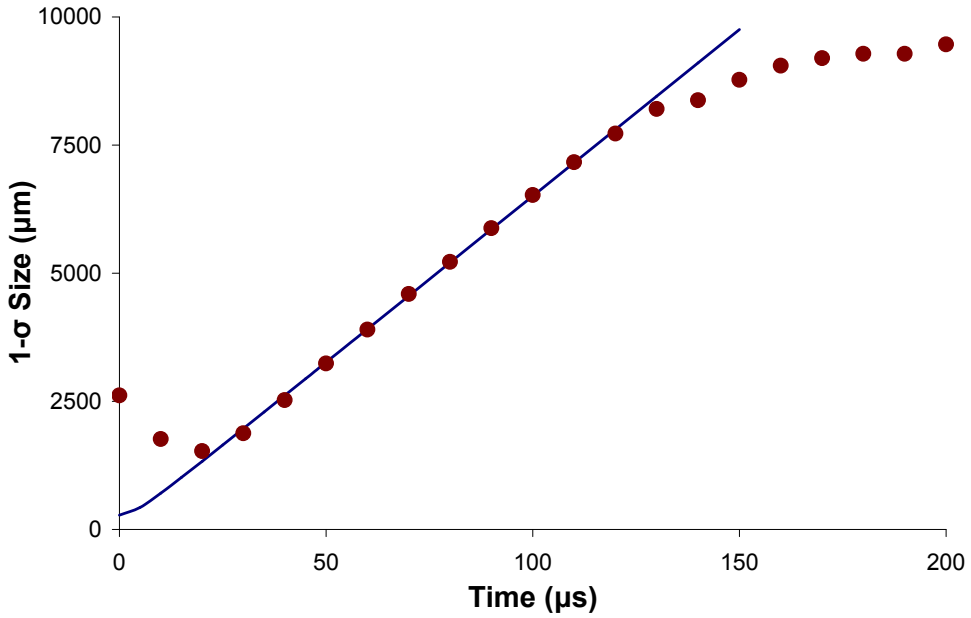

Figure A.2: The size of the ion cloud as a function of time, measured using MCP imaging. The solid blue curve without symbols is the size as approximated by $\sigma = \sqrt{v^2t^2 + \sigma_0^2}$; that is, simple ballistic expansion. The brown circles are measured 1-σ sizes of the ion cloud as a function of time, multiplied by a scaling factor due to charge lensing from the various grids.

Appendix B

Calibrating Microwave Power to Rydberg Levels

The particular microwave power required to ionize a Rydberg has a range, depending on the adiabaticity of the microwave field turn-on time [52]. Because there exists such a theoretical range in the required power, as well as a lack of equipment in the lab for directly measuring the applied microwave power in the first place and uncertainties in attenuation factors for the attenuators used, it is far more appropriate to simply calibrate the microwave power (with various attenuators) using the Rydbergs themselves.

By detuning the green photon in the photonionization process such that the final energy state is below the ionization threshold, we can actually target specific Rydberg levels, creating a Rydberg gas. Typically these gases quickly evolve into a plasma [18, 19, 20, 21, 22]; this is actually how we verify the green pulse is on resonance for the transition to a particular Rydberg level, since if the photon is tuned to a final energy between two Rydberg levels, no plasma forms. Due to the $1/N^2$ scaling of Rydberg binding energies, it is simple to identify what N-level is excited by the green pulse by scanning the green frequency and identifying several adjacent N-levels.

After setting the green frequency to create Rydbergs of a particular N-level, we strongly attenuate the green ionization beam, greatly reducing the number of

Rydbergs created. The resulting Rydberg gas has too low of a density to begin the avalanche ionization process, so plasma creation is strongly suppressed. This provides a small sample of Rydbergs with a well-defined N-level.

Immediately after the creation of the Rydberg sample, we apply microwave pulses while varying the attenuation values (using our collection of manually variable attenuators - one variable in steps of 1 dB, the other variable in steps of 10, and noting all such attenuators have some frequency dependence, so that such calibration is required for the 2.4 GHz we operate at) in the microwave system. The microwave pulse is attenuated more and more until no Rydbergs are detected; at this point, the power in the microwave field required to ionize a particular Rydberg level is determined; see Fig. B.1.

Additional calibration is needed for our high-speed voltage-controlled attenuator. We repeat the calibration procedure described above, but remove the manually controlled variable attenuators and replace them with the voltage-controlled attenuator. We then vary the voltages and determine the useful voltage-N_{min} calibration curve, as shown in Figure B.2.

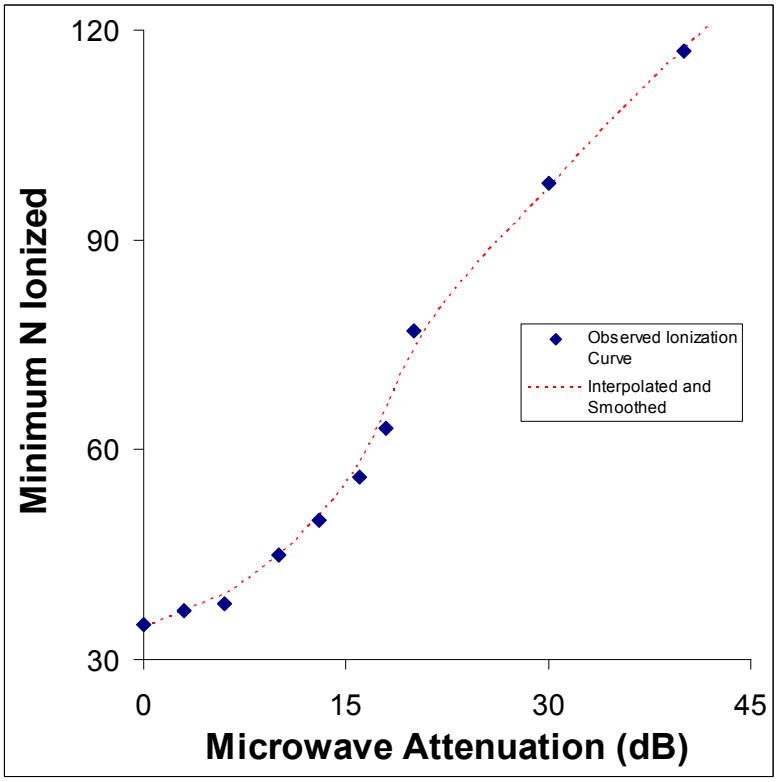

Figure B.1: Calibration of our microwave system (microwave source, closed microwave switches, amplifier, and fixed-value attenuators). At each attenuated power level (unattenuated power is estimated to be 14 dBm), the minimum Rydberg N-level observed to be successfully ionized is determined. Using the measured points, we interpolate between the points and smooth the resulting curve to give a more continuous (and useful) calibration curve.

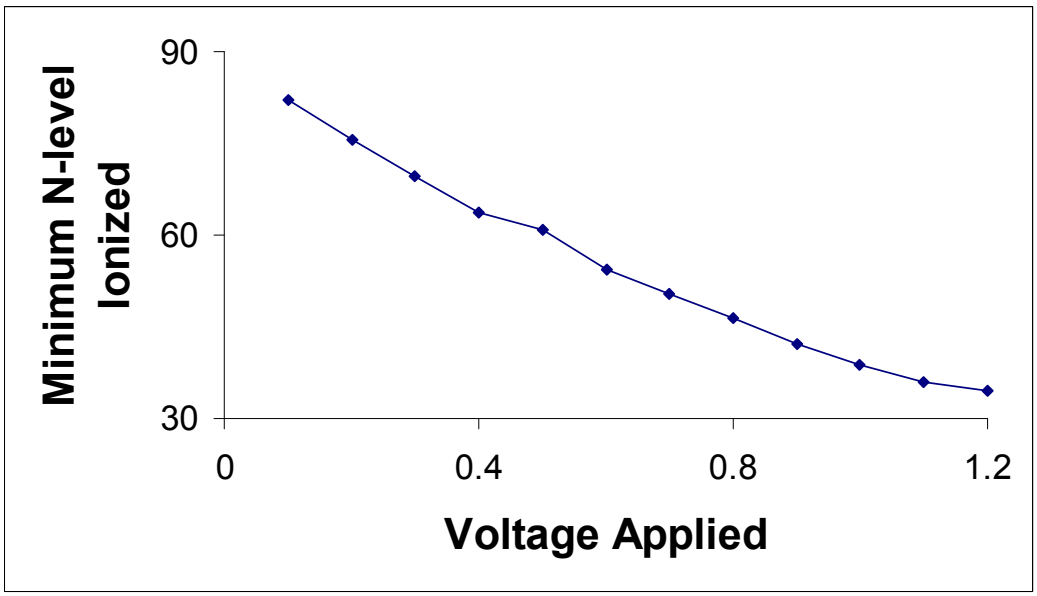

Figure B.2: Calibration of our microwave system (microwave source, closed microwave switches, amplifier, and voltage-controlled attenuator). At each attenuated power level (unattenuated power is estimated to be 13 dBm), the minimum Rydberg N-level observed to be successfully ionized is determined. This attenuator has a higher baseline attenuation than the fixed attenuators, so N-levels higher than about 100 are difficult to measure since the attenuator cannot be set to a true 0 dB level. Note the nonlinearities in this attenuator actually give a reasonably linear relationship between applied voltage and observed N_{min}.

Bibliography

[1] P. Mansbach and J. Keck, *Monte Carlo trajectory calculations of atomic excitation and ionization by thermal electrons*, Phys. Rev. **181**, 275 (1969).

[2] T. C. Killian, S. Kulin, S. D. Bergeson, L. A. Orozco, C. Orzel, and S. L. Rolston, *Creation of an Ultracold Neutral Plasma*, Phys. Rev. Lett. **83**, 4776 (1999).

[3] Matthew S. Walhout, Ph.D. Dissertation, University of Maryland, 1994.

[4] H. J. Metcalf and P. van der Straten, *Laser Cooling and Trapping* (Springer-Verlag New York, 1999).

[5] E. Raab, M. Prentiss, A. Cable, S. Chu, and D. Pritchard, *Trapping of Neutral-Sodium Atoms with Radiation Pressure*, Phys. Rev. Lett. **59**, 2631 (1987).

[6] J. Dalibard and C. Cohen-Tannoudji, *Laser Cooling Below the Doppler Limit by Polarization Gradients*, J. Opt. Soc. Am. B **6**, 2023 (1989).

[7] S. Kulin, T. C. Killian, S. D. Bergeson, and S. L. Rolston, *Plasma Oscillations and Expansion of an Ultracold Neutral Plasma*, Phys. Rev. Lett. **85**, 318 (2000).

[8] X. L. Zhang, R. S. Fletcher, S. L. Rolston, P. N. Guzdar, and M. Swisdak, *Ultracold Plasma Expansion in a Magnetic Field*, submitted to Phys. Rev. Lett. in December 2007.

[9] F. Robicheaux and J. D. Hanson, *Simulated Expansion of an Ultra-Cold, Neutral Plasma*, Phys. Plasmas **10**, 2217 (2003).

[10] D. Feldbaum, N. V. Morrow, S. K. Dutta, and G. Raithel, *Coulomb expansion of laser-excited ion plasmas*, Phys. Rev. Lett. **89**, 173004 (2004).

[11] S. G. Kuzmin and T. M. O'Neil, *Numerical simulation of ultracold plasma: How rapid intrinsic heating limits the development of correlation*, Phys. Rev. Lett. **88**, 65003 (2002).

[12] F. Robicheaux and J. D. Hanson, *Simulation of the Expansion of an Ultracold Neutral Plasma*, Phys. Rev. Lett. **88**, 055002 (2002).

[13] T. Pohl, T. Pattard, and J. M. Rost, *Coulomb crystallization in expanding laser-cooled neutral plasmas*, Phys. Rev. A **92**, 155003 (2004).

[14] T. Pohl, T. Pattard, and J. M. Rost, *Influence of electron-ion collisions on Coulomb crystallization of ultracold neutral plasmas*, J. Phys. B **38**, S343 (2005).

[15] T. B. Mitchell, J. J. Bollinger, X. P. Huang, W. M. Itano, and D. H. E. Dubin, *Direct observations of the structural phases of crystallized ion plasmas*, Phys. Plasmas **6**, 1751 (1999).

[16] C. E. Simien, Y. C. Chen, P. Gupta, S. Laha, Y. N. Martinez, P. G. Mickelson, S. B. Nagel, and T. C. Killian, *Using Absorption Imaging to Study Ion Dynamics in an Ultracold Neutral Plasma*, Phys. Rev. Lett. **92**, 143001 (2004).

[17] E. A. Cummings, J. E. Daily, D. S. Durfee, and S. D. Bergeson, *Flourescence Measurements of Expanding Strongly-coupled Neutral Plasmas*, Phys. Rev. Lett. **95**, 235001 (2005).

[18] M. P. Robinson, B. L. Tolra, N. W. Noel, T. F. Gallagher, and P. Pillet, *Spontaneous Evolution of Rydberg Atoms into an Ultracold Plasma*, Phys. Rev. Lett. **85**, 4466 (2000).

[19] T. Pohl, T. Pattard, and J. M. Rost, *Plasma Formation from Ultracold Rydberg Gases*, Phys. Rev. A **68**, 010703 (2003).

[20] W. Li, M. W. Noel, M. P. Robinson, P. J. Tanner, T. F. Gallagher, D. Comparet, B. L. Tolra, N. Vanhaecke, T. Vogt, N. Zahzam, P. Pillet, and D. A. Tate, *Evolution Dynamics of a Dense Frozen Rydberg Gas to Plasma*, Phys. Rev. A **70**, 042713 (2004).

[21] N. Vanhaeckes, D. Comparet, D. A. Tate, and P. Pillet, *Ionization of Rydberg Atoms Embedded in an Ultracold Plasma*, Phys. Rev. A **71**, 013416 (2005).

[22] W. Li, P. J. Tanner, and T. F. Gallagher, *Dipole-Dipole Excitation and Ionization in an Ultracold Gas of Rydberg Atoms*, Phys. Rev. Lett. **94**, 173001 (2005).

[23] G. Gabrielse, N. S. Bowden, P. Oxley, A. Speck, C. H. Storry, J. N. Tan, M. Wessels, D. Grzonka, W. Oelert, G. Schepers, T. Sefzick, J. Walz, H. Pittner, T. W. Hansch, and E. A. Hessels, *Background-Free Observation of Cold Antihydrogen with Field-Ionization Analysis of Its States*, Phys. Rev. Lett. **89**, 213401 (2002).

[24] M. Amoretti, C. Amsler, G. Bonomi, A. Bouchta, P. Bowe, C. Carraro, C. L. Cesar, M. Charlton, M. J. T. Collier, M. Doser, V. Filippini, K. S. Fine, A. Fontana, M. C. Fujiwara, R. Funakoshi, P. Genova, J. S. Hangst, R. S. Hayano, M. H. Holzscheiter, L. V. Jorgensen, V. Lagomarsino, R. Landua, D. Lindelof, E. L. Rizzini, M. Macri, N. Madsen, G. Manuzio, M. Marchesotti, P. Montagna, H. Pruys, C. Regenfus, P. Riedler, J. Rochet, A. Rotondi, G. Rouleau, G. Testera, A. Variola, T. L. Watson, and D. P. van der Werf, *Production and detection of cold antihydrogen atoms*, Nature **419**, 456 (2002).

[25] D. O. Gericke and M. S. Murillo, *Disorder-induced heating of ultracold plasmas*, Contributions to Plasma Physics **43**, 298 (2003).

[26] Y. C. Chen, C. E. Simien, S. Laha, P. Gupta, Y. N. Martinez, P. G. Mickelson, S. B. Nagel, and T. C. Killian, *Electron Screening and Kinetic-Energy Oscillations in a Strongly Coupled Plasma*, Phys. Rev. Lett. **93**, 265003 (2004).

[27] L. Spitzer, *Physics of Fully Ionized Gases* (John Wiley and Sons, 1962).

[28] T. Pohl, T. Pattard, and J. M. Rost, *Kinetic modeling and molecular dynamics simulation of ultracold neutral plasmas including ionic correlations*, Phys. Rev. A **70**, 033416 (2004).

[29] T. Pohl, T. Pattard, and J. M. Rost, *Relaxation to non-equilibrium in expanding ultracold neutral plasmas*, Phys. Rev. Lett. **94**, 205003 (2005).

[30] S. Mazevet, L. A. Collins, and J. D. Kress, *Evolution of Ultracold Neutral Plasmas*, Phys. Rev. Lett. **88**, 055001 (2002).

[31] S. G. Kuzmin and T. M. O'Neil, *Numerical simulation of ultracold plasmas*, Phys. Plasmas **9**, 3743 (2002).

[32] J. L. Roberts, C. D. Fertig, M. J. Lim, and S. L. Rolston, *Electron Temperature of Ultracold Plasmas*, Phys. Rev. Lett. **92**, 253003 (2004).

[33] P. Gupta, S. Laha, C. E. Simien, H. Gau, J. Castro, T. C. Killian, and T. Pohl, *Electron-temperature evolution in expanding ultracold neutral plasmas*, Phys. Rev. Lett. **99**, 075005 (2007).

[34] S. D. Bergeson and R. L. Spencer, *Neutral-plasma Oscillations at Zero Temperature*, Phys. Rev. E **67**, 026414 (2003).

[35] L. Tonks, *The High Frequency Behavior of a Plasma*, Phys. Rev. **37**, 1458 (1931).

[36] A. Dattner, *Resonance Densities in a Cylindrical Plasma Column*, Phys. Rev. Lett. **10**, 205 (1963).

[37] D. Bohm and E. P. Gross, *Theory of Plasma Oscillations. A. Origin of Medium-Like Behavior*, Phys. Rev. **75**, 1851 (1949).

[38] J. How and H. A. Blevin, *A Simplified Theory for Tonks-Dattner Resonances in Cylindrical Plasmas*, J. of Phys. D **9**, 1123 (1976).

[39] R. S. Fletcher, X. L. Zhang, and S. L. Rolston, *Observation of Collective Modes of Ultracold Plasmas*, Phys. Rev. Lett. **96**, 105003 (2006).

[40] F. Robicheaux, private communication, 2006-2007.

[41] R. S. Fletcher, X. L. Zhang, and S. L. Rolston, *Using Three-Body Recombination to Extract Electron Temperatures of Ultracold Plasmas*, Phys. Rev. Lett. **99**, 145001 (2007).

[42] Y. Hahn, *Plasma density effects on the three-body recombination rate coefficients*, Phys. Lett. A **231**, 82 (1997).

[43] L. Vriens and A. H. M. Smeets, *Cross-section and rate formulas for electron-impact ionization, excitation, deexcitation, and total depopulation of excited atoms*, Phys. Rev. A **22**, 940 (1980).

[44] Y. Hahn, *Electron-ion recombination processes - an overview*, Rep. Prog. Phys. **60**, 691 (1997).

[45] M. E. Glinsky and T. M. O'Neil, *Guiding center atoms: three-body recombination in a strongly magnetized plasma*, Phys. Fluids B **3**, 1279 (1991).

[46] T. Pohl and T. Pattard, *Electron-ion recombination in strongly coupled cold plasmas under nonequilibrium conditions*, Journal of Physics A **39**, 4571 (2006).

[47] T. C. Killian, M. J. Lim, S. Kulin, R. Dumke, S. D. Bergeson, and S. L. Rolston, *Formation of Rydberg Atoms in an Expanding Ultracold Neutral Plasma*, Phys. Rev. Lett. **86**, 3759 (2001).

[48] H. Gao, D. R. DeWitt, R. Schuch, W. Zong, S. Asp, and M. Pajek, *Observation of enhanced electron-ion recombination rates at very low energies*, Phys. Rev. Lett. **75**, 4381 (1995).

[49] M. J. Seaton, *Radiative Recombination of Hydrogen Ions*, Mon. Not. Roy. Astron. Soc. **119**, 81 (1959).

[50] W. Graham, W. Fritsch, Y. Hahn, and J. A. Tanis, *NATO ASI Series B: Physics, Recombination of Atomic Ions, Vol. 296* (Plenum, 1992).

[51] J. Stevefelt, J. Boulmer, and J.-F. Delpech, *Collisional-radiative recombination in cold plasmas*, Phys. Rev. A **12**, 1246 (1975).

[52] T. F. Gallagher, *Rydberg Atoms* (Cambridge University Press, 1994).

[53] Y. B. Zel'dovich and Y. P. Raizer, *Physics of Shock Waves and High-Temperature Hydrodynamic Phenomena* (Academic Press, 1966).

[54] E. Hinnov and J. G. Hirschberg, *Electron-Ion Recombination in Dense Plasmas*, Phys. Rev. **125**, 795 (1962).

[55] N. D'Angelo and N. Rynn, *Diffusion and Recombination of a Highly Ionized Cold Plasma in a Magnetic Field*, Phys. Fluids **4**, 1303 (1961).

[56] S. X. Hu, *Three-Body Recombination of Atomic Ions with Slow Electrons*, Phys. Rev. Lett. **98**, 133201 (2007).

[57] T. Pohl, private communication and based on his manuscript *Rydberg atom formation in ultracold plasmas: Small energy transfer with large consequences* submitted to Phys. Rev. Lett. in late 2007.

[58] A. F. Kuckes, R. W. Motley, E. Hinnov, and J. G. Hirschberg, *Recombination in a helium plasma*, Phys. Rev. Lett. **6**, 337 (1961).

[59] M. Pajek and R. Schuch, *Plasma Effects in Three-body Recombination of High-Z Bare Ions with Electrons*, Physica Sripta **T80**, 307 (1999).

[60] H. Gao, R. Schuch, W. Zong, E. Justiniano, D. R. DeWitt, H. Lebius, and W. Spies, *Energy and charge dependence of the rate of electron-ion recombination in cold magnetized plasmas*, J. Phys. B **30**, L499 (1997).

[61] L. Vriens and A. H. M. Smeets, *Cross-section and rate formulas for electron-impact ionization, excitation, deexcitation, and total depopulation of excited atoms*, Phys. Rev. A **22**, 940 (1980).